Efficient design of a Thermally Tunable Directional Coupler for Integrated Silicon Photonics

A THESIS

submitted by

J.SRINATH – EE13B125

in partial fulfillment of the requirements
for the award of the degree of

BACHELOR OF TECHNOLOGY

DEPARTMENT OF ELECTRICAL ENGINEERING
INDIAN INSTITUTE OF TECHNOLOGY MADRAS.

June 2017

This is to certify that the thesis titled **Efficient design of a Thermally Tunable Directional Coupler for Integrated Silicon Photonics** , submitted by **J.Srinath**, to the Indian Institute of Technology, Madras, for the award of the degree of **Bachelor of Technology**, is a bona fide record of the research work done by him under our supervision. The contents of this thesis, in full or in parts, have not been submitted to any other Institute or University for the award of any degree or diploma.

Dr. Bijoy Krishna Das
Research Guide
Associate Professor
Dept. of Electrical Engineering
IIT-Madras, 600 036

Place: Chennai, India

Date: Tue 27th Jun, 2017

"The journey of a thousand miles begins with one step."
-Lao Tzu

ACKNOWLEDGEMENTS

A written acknowledgement is not sufficient to express the sheer magnitude of gratitude I have toward the various people who have helped me grow both technically and as a person.However, I would like to take this opportunity to sincerely thank my guide Dr. Bijoy Krishna Das for kindling and nurturing my interest in Silicon Photonics. In addition to to being a great teacher and guide, he has been a constant source of encouragement and support in all my academic endeavors and has been tremendously understanding. His constant guidance and care is testament to the great mentor he is.

I would also like to thank the entire IOLAB group who made me feel like a part of a big family. In addition to being helpful seniors, they have also become great friends. A special thanks to Riddhi Nandi, Sreevatsa Kurudi, Sumi Sterin, Ramesh, Saket and Sujith. My project and general stay in the the group has been memorable to say the least and the memories I made here will stay with me and be cherished. I would also like to thank Parimal, Sooraj, Meenu for being so approachable and for helping me with any problems.

I would also like to thank my friends Daniel Viju, Aakash Urangapuli,Vigneshram,Mukesh Krishnan, Arun and Bacchu Smaran Raj for being there when it mattered and for cheering me up and encouraging me through the long journey that has been my B.Tech. I would also like to thank my batch-mates for making this experience truly memorable and for adding great fun and joy to my life in 'Insti'.

Finally, I would like to thank my parents and my sisters for supporting in me in all my endeavors, for taking the good with the bad and for molding me into who I am today.

ABSTRACT

Due to its small geometrical structure and compatibility with CMOS technology, the Silicon photonic rib waveguide based platform holds great promise with regard to the integration of electronic and photonic components. There is also a tremendous need for active devices to demonstrate more complex, adaptable and multi-functional devices. The Tunable Directional Coupler (TDC) is one such device that can be used as a power-splitter, modulator and can also be used in Ring resonator devices amongst other uses.Though, there exist good functional designs, most of the designs are based on over-clad heaters. The possibility of compact and more energy efficient designs exist using laterally placed heaters. A method of Numerical analysis is also required to study these designs.

In the work presented, a method of numerical analysis is proposed to study the TDC performance. This is first benchmarked by applying the method to an existing scheme. New designs based on laterally offset heaters are studied.Based on the observations made and trends studied, a new design which consists of 'Optically coupled but Thermally decoupled' rib waveguides is also proposed. This design is analyzed and optimized through the method proposed earlier .All the simulations for optimization of the design are executed using Lumerical MODE solutions, Lumerical DEVICE and COMSOL multiphysiscs. The device was designed for TE polarization and for a wavelength of $1.55\mu m$ (C-band). The device layer thickness is 220 nm ($2\mu mBOX$) and the slab heights considered are 130 nm and 50 nm. A term tunability (Γ) is also defined which is the slope of the $K - P_D$ plot in the region of interest ($P_D - 10 : 30mW$). Tunabilities of upto $50W^{-1}$ is obtained for the proposed design ($h_{slab} = 50$) which is greater than the tunability of the existing design ($24.19W^{-1}$) and K as low as 0.1 is obtained for the proposed design which is less than K for the existing design (0.46).The estimated response times are also found to be marginally lesser than the existing design and predict that the overall response time for the proposed design will be less than $10\mu s$.

TABLE OF CONTENTS

LIST OF TABLES

LIST OF FIGURES

ABBREVIATIONS

Acronyms

C-Band	Conventional wavelength band ($\lambda \sim 1527$ to 1567 nm)
L-Band	Long wavelength band ($\lambda \sim 1567$ to 1607 nm)
WDM	Wavelength-division-multiplexing
DWDM	Dense wavelength-division-multiplexing
CMOS	Complementry Metal Oxide Semiconductor
DI	De-ionized (water)
FEM	Finite Element Method
FSR	Free Spectral Range
ICP	Inductively Coupled Plasma
MZI	Mach Zehnder Interferometer
TDC	Tunable Directional Coupler
PPR	Positive Photo Resist
LCRW	Large Cross-section Rib Waveguide
RCRW	Reduced Cross-section Rib Waveguide
PhW	Photonic Wire Waveguide
RIE	Reactive Ion Etching
SEM	Scanning Electron Microscope
SMF	Single Mode Fiber
SOI	Silicon-On-Insulator
TE	Transverse Electric (polarization)
TM	Transverse Magnetic (polarization)
EMI	Electromagnetic interference
UV	Ultra-Violet

Units

dB	decibel
dBm	decibel milli-watt
mW	milli watt
μW	micro watt
μm	micrometer
ns	nano Second
μs	micro second
sccm	standard cubic centimeter per minute
mTorr	milli-Torr (of pressure)
mbar	milli-Bar (of pressure)
ml	milli-liter (of fluid)

NOTATION

$\mathbf{n}$	Refractive index
$\mathbf{n}_{eff}$	Effective refractive index
$\boldsymbol{\epsilon}$	Permitivity
$\boldsymbol{\lambda}$	Wavelength
$\boldsymbol{\beta}$	Propagation constant
$\boldsymbol{\phi}$	Phase of the EM wave
$\mathbf{L}$	Length (refers to device length, component length)
$\boldsymbol{\Gamma}$	Tunability
$\boldsymbol{\alpha}$	Loss per unit length

CHAPTER 1

Introduction

1.1 Background

As the geometries of the VLSI chips become smaller and denser and as computations become faster and more complex, the capacity of electronic circuits is being outstripped. The connections simply cannot handle electric signals fast enough and process them. Exploiting the fact that light travels faster than electronic signals, we can replace the electronic interconnects with optical interconnects. Optical interconnects in the form of on chip waveguides offer an excellent alternative with the advantage of higher bandwidth, lesser delays and lower power dissipation. Due to its transparency in the range of optical wavelengths, Silicon can be used to make these optical interconnects which offer smaller delay and better resistance to Electromagnetic interference (EMI) as compared to the conventional electrical interconnects.

Silicon photonics, which is associated with signal generation, processing, transmission and detection where the light is carried in Silicon based components has established itself as the dominant platform for on-chip optical interconnects.

Waveguides are the most fundamental components for all of the Silicon Photonic devices. These devices work on the Silicon on Insulator (SOI) platform.The Silicon layer is sandwiched between the buried insulator and top cladding of air. As the refractive indices of these claddings are lower than that of Silicon, propagation of Electromagnetic waves in the waveguides is possible on the basis of total internal reflection.

In a typical rib waveguide (see fig 1.1),light is confined in two directions, in both the x and y direction and is guided along the propagation direction z. Pure TE and TM modes do do not exist in these waveguides, instead we have hybrid modes called TE like modes (E_x and H_y dominate) and TM like modes (E_y and H_x dominate). The

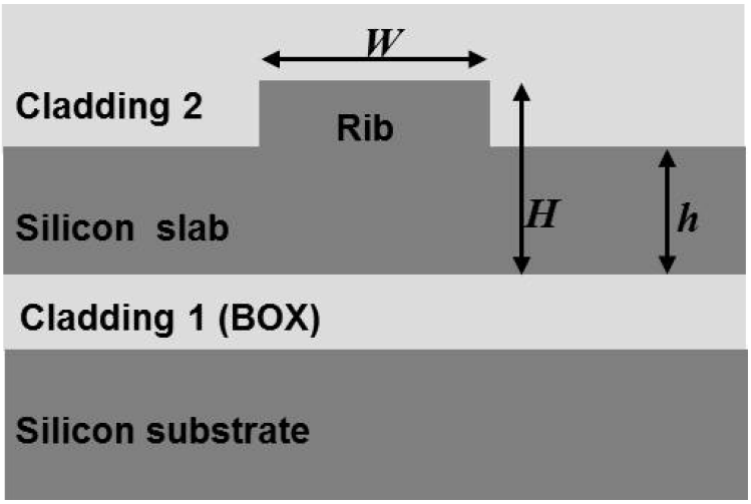

Figure 1.1: Schematic cross-sectional view of a typical optical waveguide geometry in SOI substrate: BOX - buried oxide, W - waveguide width, H - rib height and h - slab heights

modes that propagate through these structures are termed as 'guided modes'. The advantage of these waveguides especially at the sub-micron dimensions exist in the relatively tighter confinement of modes allowing for compact designs with minimal losses. While waveguides act as the interconnects, other components both 'active' and 'passive' are required to create functioning integrated components. Passive components are components whose device characteristics are fixed like Interferometers, directional couplers. Whereas active components are those whose characteristics can be changed on application of external input like Modulators and the active versions of the passive components (Tunable Directional Coupler).

Active control of guided modes is possible via strong plasma dispersion and thermo-optic effects [1].Plasma dispersion effect is mainly used to demonstrate high speed modulators [2] [3], switches [4] etc. However, the large thermo-optic coefficient of Silicon ($\frac{dn}{dT} = 1.86 \times 10^{-4} K^{-}1$) is frequently used for an energy efficient switching[5] [6],routing [7], tuning [8], reconfigurable circuits [9] etc. Thermo-optic effect, albeit inherently slower compared to plasma dispersion effect is essentially lossless leading to huge prospects in optical interconnect and microwave photonics applications[10].

Tunable integrated power-splitting devices have been deeply investigated since the early stages of integrated optics, including thermally or electro-optically actuated directional couplers (DCs) [11] and multimode interference (MMI) couplers[12]. In silicon

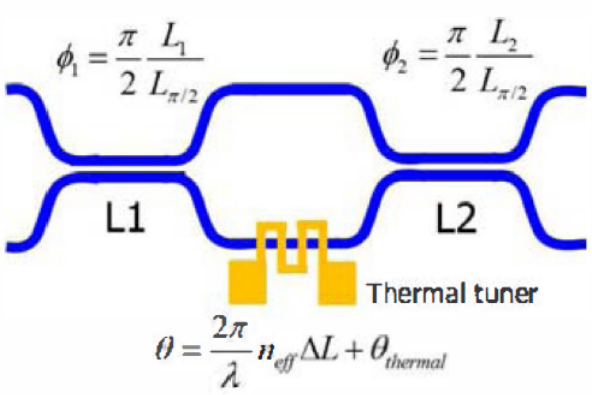

Figure 1.2: Schematic top view of the MZI based broadband TDC where the heater is placed on top of on of the MZI arms to perturb MZI response

photonics the most common approach to realize a tunable coupler exploits a thermally actuated balanced Mach-Zehnder interferometer (MZI) [13],[14].Although being simple to implement and widely tunable with a moderate electric power consumption, the MZI tunable coupler requires a pair of 3 dB splitters, thus resulting in a larger device and higher insertion loss. A compact tunable directional coupler (TDC) consisting of a single silicon photonic DC driven by the transverse temperature gradient induced by a laterally shifted heater has also been proposed and demonstrated. This design is discussed in chapter 1.Most of the instances of thermo-optic switches and devices are based on over-clad heaters [8].

For example, an MZI based broadband TDC [15] has been recently been demonstrated (shown in figure 1.2). It consists of an unbalanced MZI and a heater on one arm. The heater creates a phase mismatch and therein changes the interference pattern and consequently power splitting ratio. The broadband component or the flat wavelength response is achieved by optimizing ΔL in the phase difference term. While it provides a relatively wavelength independent response, it is large and insertion losses are relatively higher. Also, fabrication is a lot more complex.Thus, a better more compact design is required.

While, overclad heater based devices provide good performances, response time and energy efficiencies are areas of improvement. This is addressed by using lateral heaters. In lateral heaters [16],[17] metal is deposited directly on slab region adjacent to rib waveguide, ensuring better usage of thermal energy. Moreover, the slab

forms a conductive path to dissipate heat faster, leading to lower response time as well ($\tau_{res} < 10\mu s$).The use of lateral heater for a Tunable directional coupler (TDC) design represents a possibility to obtain better overall device performance.

While the paper on TDC [8] discusses overclad heater based Tunable Directional Coupler and discusses the possibility for numerical analysis showing a few simulation results, a detailed framework or formulation was not laid out. This is very important, since the framework laid out will enable us to evaluate any heater based tuning scheme used for directional couplers. The extension of this method of numerical analysis using FDM (Finite Difference Methods) and FEM (Finite Element Method) solvers to evaluate the performance of lateral heater designs also represents an exciting avenue to explore. This work combines the need for a codified framework with the possibility of obtaining a better TDC to produce useful simulation based performance analyses and a better device design.

1.2 Formulation of the Solid Heat-transfer problem

Joule heating effect is most commonly used to achieve thermo-optic modulation in Silicon. The governing heat equation for the conduction is solids is given by:

$$-\nabla \cdot (k\nabla T) + \rho C_p \frac{dT}{dt} = Q_s \tag{1.1}$$

where k is the thermal conductivity of the material, T is the Temperature, ρ is the density of the material, C_p is the heat capacity at constant pressure of the material,t is the time and Q_s is the density of the heat power generation. The variation of the material properties with the local temperature (T) also have to be considered, though amongst the material properties for Silicon, only k shows a significant variation with temperature while the variations in C_p and ρ can be neglected [18] in the temperature range of $300K - 500K$. Silica, in general does not react to temperature changes, so variation its material properties can also be neglected while modeling.The equation 1.1 can be basically divided into two parts, the first part deals with the temperature distribution due to the applied heat and the second part deals with the portion of heat

required to raise the temperature by a certain amount. This equation is time dependent, but at steady state, the time dependence vanishes and the equation becomes:

$$-\nabla \cdot (k\nabla T) = Q_s \tag{1.2}$$

This is called the Fourier's law of thermal conduction and is used to solve for the temperature profile at steady state.For the Joule electromagnetic heating problem Q_s term is generally replaced by $\nabla \cdot J$, where J is the current density. But this essentially means that the potential difference must be given as an input to the model. We are interested in the action of the power dissipated (P_D) in the resistive heater and using the Joule heating model does not give a direct relation between the power dissipated at the source/resistor and the temperature profile. The translational symmetry (heat conduction is symmetric along direction of current) flow of the problem allows us to convert this Joule heating problem into a solid heat transfer problem in two dimensions. The Q_s is replaced by the power dissipated per unit volume of the source.

This idea of exploiting the translational symmetry to convert the 3-D Joule heating problem into the 2-D solid heat-transfer has already been leveraged in the papers [19] and [16].The uniformly distributed heat source has also been utilized in [16] and [20] to solve the heat-transfer problem. The 2-D formulation is extremely important because it allows us to study the Thermo-optic tuning from a modal viewpoint using MODE solutions rather than a less intuitive Finite Difference Time method (3-D) viewpoint. Lumerical MODE solutions finds the modal properties for a particular cross-section.This makes it imperative for the Temperature profile to be in 2-D. This formulation is also computationally very efficient.

1.3 Directional Coupler

The Directional Coupler is a very important component in Silicon photonics and is regularly used as a power splitter and also in MZI's.Directional couplers (DCs) which consist of two single-mode waveguides in close proximity of each other for a finite length. The schematic top view of a DC is shown in Figure 1.3.When the waveguide separation

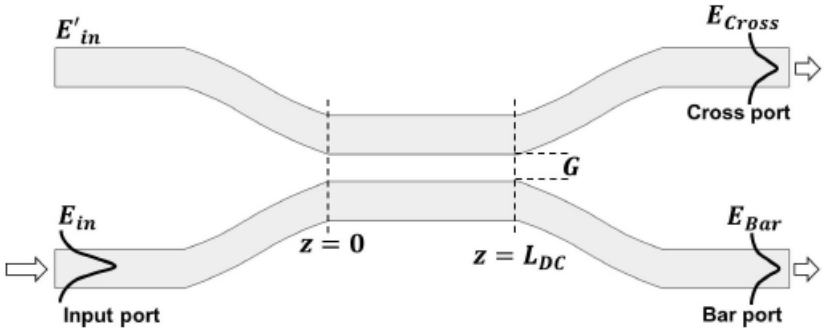

Figure 1.3: Schematic top view of a 2×2 DC: L_DC - length of DC, G - coupled waveguideseparation, Ein, EBar and ECross are electric field amplitudes at Input,Bar and Cross ports

(G) is small enough such that the evanescent tails of the guided modes of the waveguides overlap each other causing the exchange of power between waveguides. The efficiency of coupling depends on the strength of evanescent field interaction between the coupled waveguides.The working principle of a DC can be explained by supermode analysis [21]. supermode analysis decomposes the input power into two independent components. The modes associated with these components are the symmetric and antisymmetric modes. In general the input field strength is equally distributed between the two modes.The mode profiles of the symmetric and antisymmetric modes are shown in figure and the corresponding schematic of visualizing input in terms of these components are shown in figure Essentially based on the supermode theory, the coupling factor or κ can be written as:

$$\kappa = \pi \Delta N / \lambda \tag{1.3}$$

$$\Delta N = n_{sym} - n_{antisym} \tag{1.4}$$

where n_sym and $n_{antisym}$ are the effective indices of the symmetric and antisymmetric modes respectively [21]. this is the same coupling fraction from the coupled mode theory. The coupled mode theory of the waveguide approaches the power exchange in directional coupling from an index perturbation viewpoint. The coupled mode equations are as given follows[22]:

$$\frac{dA(z)}{dz} = -j\kappa B(z) e^{j\Delta\beta z} \tag{1.5}$$

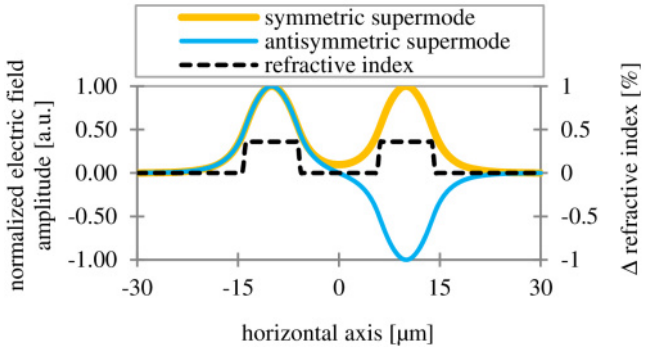

(a)

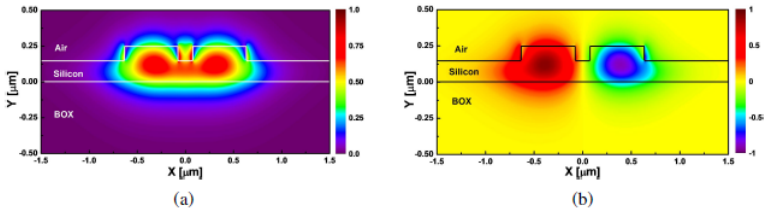

(b)

Figure 1.4: (a)Representation of input given to 1 waveguide in terms of the supermodes(b)Calculated electric field profiles for [a] symmetric and [b]] antisymmetric modes of a DC with W = 560 nm, H = 250 nm, h = 150 nm and G = 150nm.

$$\frac{dB(z)}{dz} = j\kappa^* A(z) e^{-j\Delta\beta z} \tag{1.6}$$

where A(z) and B(z) represent the modulations in the field intensities of the guided modes that are involved in coupling in the waveguides and $\Delta\beta$ represents the phase mismatch term or the difference in the propagation constants of the respective waveguides (independently evaluated). Solving these equations, the power fraction in the cross coupled port at the coupling length (L_c) can be found out to be[22]:

$$K = \frac{|\kappa|^2}{S^2}(\sin(SL_c))^2 \tag{1.7}$$

We evaluate κ from the supermode theory and use the corresponding value in the coupled mode equation to get the power splitting ratio. From the equations given above we can also deduce that the coupling length (L_c) is given by $\frac{\lambda}{2\Delta N}$ where ΔN is as given in 1.3. Thus all the DC parameters are obtained as a function of symmetric and antisymmetric mode indices.

1.4 Research Objective

There is a need for an energy efficient TDC with a faster response time. Also, a method of analysis based on numerical methods needs to be developed to analyze the design performance.In this work, it was proposed to suggest a novel lateral heater based design, simulate and quantify its performance and to compare it with already existing designs.

1.5 Thesis Organization

The entire thesis work has been presented in three distinct chapters excluding Chapter 1 for Introduction and Chapter 5 for Conclusions.

Chapter 2 discusses the already demonstrated TDC with an overclad heater[8] and develops a formulation for the analysis of TDCs through two dimensional simulations. It also discusses the evaluation of the Tuning response of the existing overclad heater based TDC, comparing it with the results obtained in literature [8].Chapter 3 explores the TDC designs without overclad, the corresponding factors to be considered for optimization of such a design and their performance. Chapter 4 presents the proposed 'Optically coupled but Thermally decoupled design' and also discusses all aspects of the proposed device's performance including the tuning response and the response time.

CHAPTER 2

Numerical Analysis of Tunable Directional Coupler Design with Oxide Over-cladding

2.1 Device design and specifications

In order to set up a theoretical basis and to set a benchmark for the proposed framework for the Numerical Analysis for Tunable Directional Coupler (TDC), systematic 2-D thermo-optic simulations were performed to reproduce the experimental results as obtained in the paper titled "Tunable silicon Photonics directional coupler driven by a transverse temperature gradient."[8]

Figure 2.1 shows the cross-sectional sketch and top view of the device-design under consideration. A 480 nm $\times$ 220 nm silicon core waveguide (single mode guided) on a 2 μm buried oxide (BOX) under-cladding and a 700 μm bulk silicon substrate is employed. In the coupling section of the TDC, two straight waveguides are spaced by a gap distance-g, and are embedded in an oxide bi-layer formed by spun and baked Hydrogen Silsesquioxane (HSQ) and SiO_2, resulting in an over-cladding thickness of $H = 900nm$.A Ni-Cr heater with a width $W_h = 900nm$ and height $t_h = 50nm$ is placed on top of the over-cladding at a distance d, from the center of one of the coupled waveguides.The heater length is made equivalent to that of the coupling section (L_c).

The values used for the modeling parameters in the simulations are as shown below:

Materials	$\rho(\frac{Kg}{m^3})$	$C_p(\frac{J}{KgK})$	$k(\frac{W}{m^2K})$
Silicon	2330	711	163
BOX (under-clad)	2203	709	1.38
Over-clad	2203	709	1
Heater(Ni-Cr)	8400	450	11.3

Table 2.1: Modeling parameters for Thermal Simulation

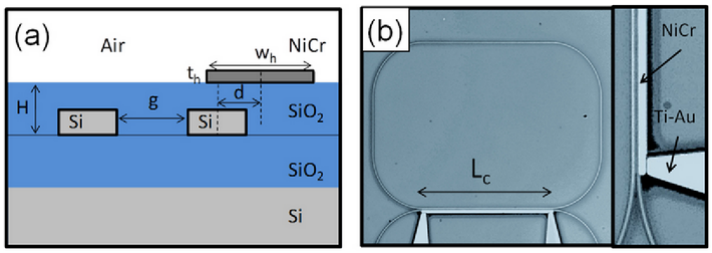

Figure 2.1: Schematic representing the design proposed [8] (a) Cross-sectional view (b)Top view

2.2 Simulation Methodology

The coupled power K between the waveguides of the TDC as mentioned earlier is given by:

$$K = \frac{|\kappa|^2}{S^2}(\sin(SL_c))^2 \tag{2.1}$$

where $S = (\kappa^2 + \frac{\Delta\beta^2}{4})^{0.5}$, κ is the field coupling coefficient, $\Delta\beta$ is the phase mismatch term and λ is the operating wavelength.

The heater introduces a temperature distribution and a corresponding refractive index distribution over the region of interest (Thermo-optic effect).This is manifested in the difference in refractive index of the two waveguides causing a phase mismatch of $\Delta\beta$. Essentially,switching the heater on induces a transverse temperature gradient ΔT proportional to the dissipated electric power P_D and provides an extra effective index difference Δn_{th} between the two waveguides that adds to the intrinsic one, Δn. In this case,the intrinsic phase mismatch is zero because the waveguide dimensions are the same for both the waveguides.

In order to quantify and compute the Thermo-optic effects due to the presence of the heater, the following general framework as shown pictorially in Figure 2.2 is followed:

1. Two dimensional thermal simulations are performed on Lumerical DEVICE using a uniform heat source enveloping the area defined as the heater. The third dimension is considered by entering the length of the simulation region in the through plane (Z-axis) into the solver.

2. This profile is then imported into Lumerical MODE solutions to compute the effect of the thermal profile on the effective indices. Firstly, both the waveguides are considered and hence we obtain the effect of the heater on the symmetric and antisymmetric modes respectively. The $n_{sym}(P_D)$ and $n_{antisym}(P_D)$ are obtained

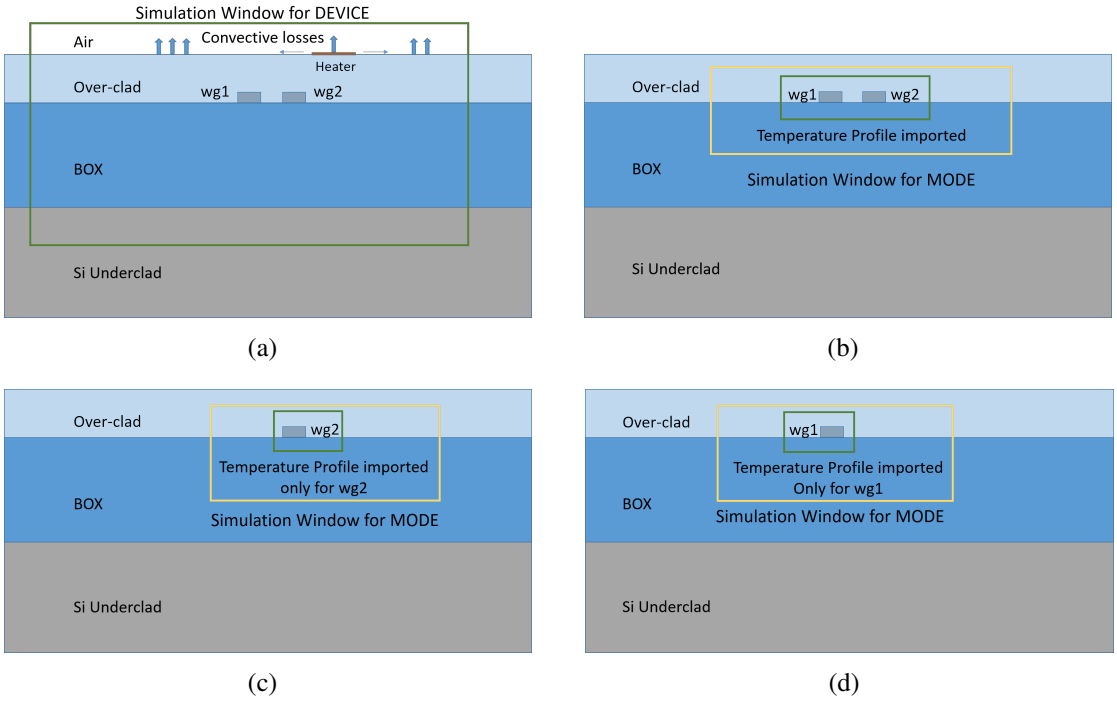

Figure 2.2: Schematic representation of the Framework for Thermo-optic Simulations: Clockwise (a) Thermal Simulation on DEVICE (b) Exporting Thermal Profile to Evaluate $\Delta N(P_D)$ (C) Exporting the thermal profile and computing effect on waveguide 1 alone (n_{wg1}) (d) Exporting the thermal profile and computing effect on waveguide 2 alone (n_{wg2})

and the corresponding $\kappa(P_D)$ is computed using the equation:

$$\kappa(P_D) = \frac{\pi \Delta N(P_D)}{\lambda} \tag{2.2}$$

where $\Delta N(P_D) = n_{sym}(P_D) - n_{antisym}(P_D)$

3. The temperature profile is again imported into MODE solutions, but the waveguides are considered separately (i.e) the effect of the dissipated power P_D is considered individually for the two constituent waveguides. The same temperature profile is imported first to compute the n_{eff} of the first waveguide in the absence of the other and vice versa. The obtained effective indices are then used to compute $\Delta\beta$ according to the following equation

$$\Delta\beta(P_D) = \frac{2\pi \Delta n(P_D)}{\lambda} \tag{2.3}$$

where $\Delta n(P_D) = n_{wg2}(P_D) - n_{wg1}(P_D)$ and $n_{wg2}(P_D)$,$n_{wg1}(P_D)$ are the new refractive indices of waveguides 2 and 1 after the application of power P_D respectively.

4. The coupled power is then computed using the values of κ and $\Delta\beta$ obtained above using the equation 2.1.The coupled power is obtained as a function of the Power dissipated (P_D).

The performance of the design is quantified mainly by the, Tunability (Γ), here is defined as as follows:

$$\Gamma = \frac{K(0) - K(P_D^{max})}{P_D^{max}} \tag{2.4}$$

where P_D^{max} is the maximum power injected into the heater during the course of either the simulation or an experimental study.

2.3 Setting up the 2-D Heat Transfer problem

2.3.1 Heat Source

The coupled Electrostatic-Heat-Transfer problem is converted into a two dimensional Heat-Transfer problem on account of translational symmetry.The heat source considered for introducing Heat power into the simulation region is a uniform heat source which uses the Solver's normalized length to consider the third dimension. The power provided (in $Watts$) is divided by the normalized length to obtain the in-plane heat flux in $Watts/m$. This normalized heat flux is then uniformly distributed across the region of interest, which in this case is the heater cross-section. Using the Uniform Heat Source allows us to consider the heater as a part of the simulation region (Temperature profile computed for the heater-region too) and allows us to effectively inject the power required into the heater. In contrast, the Power boundary condition does not consider the heater as a part of the simulation region and does not effectively inject the power required.In 2.3(b), we can see that the power is injected into the heater region and the convective heat flux condition is also considered correctly. On the other hand, in 2.3(a), we see that the complete power is not injected correctly into the simulation region; if the height of the heater is extremely small, then only half of the applied power would be injected into the simulation region.Also, we can notice that the convective heat flux condition is not applied at all. Thus, the uniform heat source is used for our simulation.

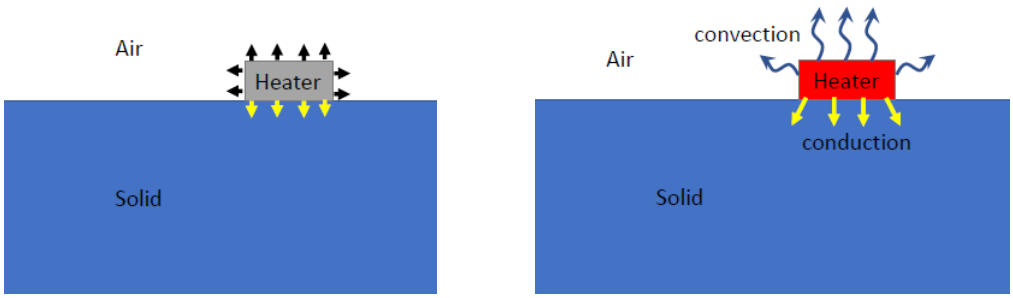

Figure 2.3: Schematic representation of Power sources [Yellow arrows indicate heat flow into simulation region] a) Power Boundary condition b) Uniform Heat Source

2.3.2 Boundary Conditions

In addition to the defined Heat Power source, boundary conditions are required to solve the differential equation based heat-Transfer problem. Here the the bottom vertical extent of the simulation window ($-y - axis$) is assumed to be at room temperature at the steady state, whereas the right and left extents of the simulation window are assumed to the thermally insulated (Heat fluxes passing out through the extents are zero).

The Interfaces between the simulation window and the atmosphere/environment are modelled by using convective heat flux boundary conditions as shown in Figure 2.4. The equation for the Heat convection boundary condition is:

$$h_{air}[T_{surface} - T_{amb}] = -k\frac{\delta T}{\delta n} \tag{2.5}$$

where h_{air} $[Watts/m^2K]$ is the convective heat constant for air,$T_{surface}$ is the temperature of the surface at any given point,$T_{ambient}$ is the ambient temperature ($= 300K$), n is the direction perpendicular to the surface and the Right hand side is the characteristic Solid heat transport equation. Essentially, this boundary condition imposes that heat conduction at the surface in a given direction is equal to heat convection in the same direction. Both sides of the equation are in units per area.

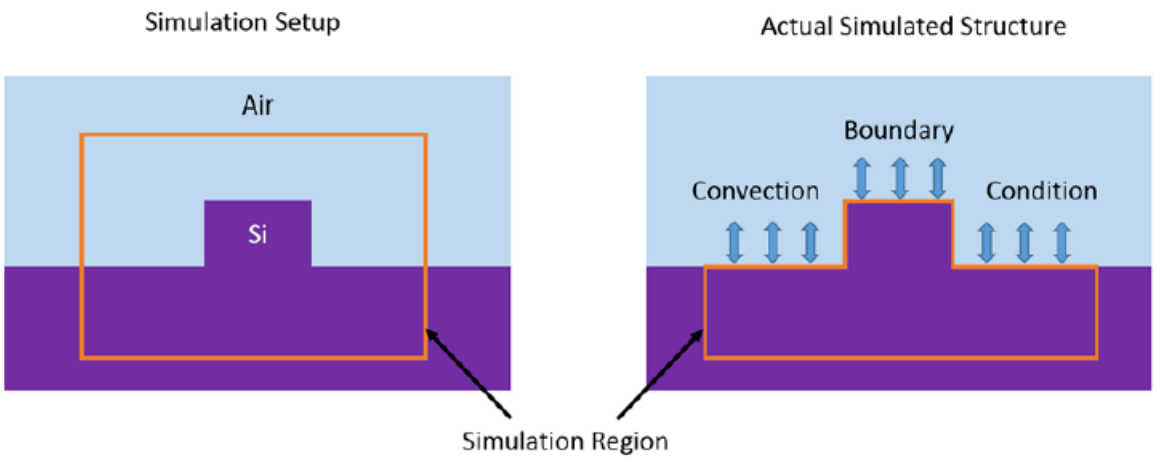

Figure 2.4: A schematic to represent the implementation of Convective heat flux boundary condition in Lumerical DEVICE

2.4 Modeling the Index perturbation due to Temperature Gradient

The material for the waveguides is defined as an index-perturbed material with the base material as Silicon-Pallik (MODE solutions). This is to include the variation of the refractive index of Silicon with Temperature. The thermo-optic coefficient of Silicon at room temperature is 1.86×10^{-4}, whereas the thermo-optic coefficient of Silica at room temperature is of the order of 10^{-6} [23]. Thus, whilst considering the effect of the temperature distribution on the local refractive index, the index is assumed to be perturbed only for Silicon, since the change in refractive index of Silica is negligibly small. The Thermo-optic coefficient($\Theta = \frac{dn}{dT}$) of Silicon is also a function of Temperature(T) and the relationship between them is as given below[24]:

$$\frac{dn}{dT} = 9.48 \times 10^{-5} + 3.47 \times 10^{-7} \times T - 1.49 \times 10^{-10} \times T^2 \qquad [K^{-1}] \qquad (2.6)$$

It is observed that Θ varies very slowly with T. Thus, intervals of $2K$ are taken to estimate the Δn as a function of T. The refractive index change with respect to the room temperature refractive index is estimated as $\Delta n(T) = n(T-a) + \alpha(T-a) \times a - n(300K)$ where a is the interval size, which is taken as 2K. The refractive index change so obtained as a function of Temperature is then imported into the material properties section of the defined index perturbed material.The waveguides are defined using this

newly defined material. This ensures that the temperature profile when imported is translated into a refractive index profile in MODE. Thus the effect of temperature on the thermo-optic coefficient is also considered.

2.5 Phonon transport limited thermal Conductivity

Another factor to include in the simulations is the dependence of the thermal conductivity of Silicon on the film thickness or the height, specifically when we are dealing with sub-micron dimensions.When the slab/rib dimensions become smaller than the characteristic mean free path (Λ) of the dominant phonon mode at any temperature ($\Lambda = 300nm$ at room temperature), phonon scattering becomes a very important aspect to consider. A phonon refers to the quanta of energy of lattice vibrations in semiconductors such as Si and Ge. Phonons can be treated as particles despite the fact that they are propagating wave packets, which carry energy across the lattice.

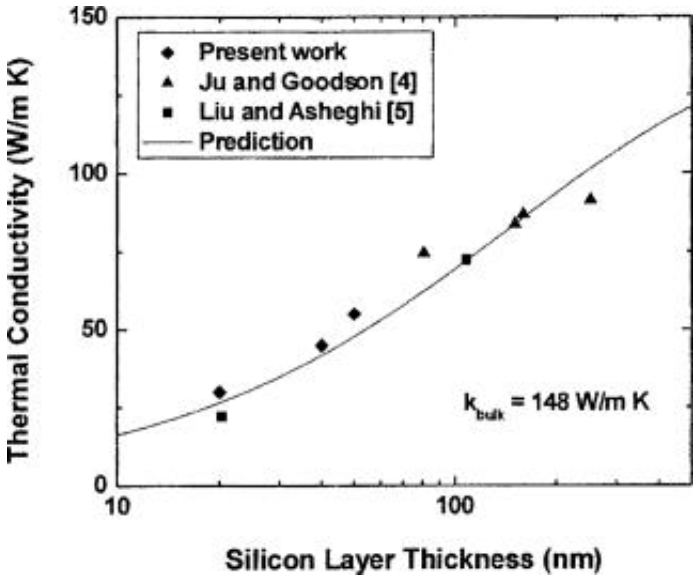

Figure 2.5: Variation of thermal conductivity (k) with film thickness ([25])

In these conditions,the Fourier equation for heat transport by itself does not hold in the strictest sense. But, there exists a workaround to solve this issue.The phonon effects mainly manifest in the form of the degradation of the thermal conductivity (k). The incorporation of this modified thermal conductivity in the Fourier equation should provide us with a good estimate of the actual Thermal transport. This idea of using the modified

thickness-dependent thermal conductivity in the Continuum transport equation (Fourier equation) has already been implemented in [16], where a thermo-optic phase shifter was designed with a design similar to our proposed design.Here, we adopt the same model where all the sub-continuum and phonon dependent effects are included in the thermal conductivity. We still use the Fourier equation.

We obtained the thickness dependent thermal conductivity values from [25]. The plot of the thermal conductivity versus length as shown in fig 2.5 was digitized using the 'WebPlotDigitizer' ([26]) to get the precise values of thermal conductivity as mentioned in the paper.

The thermal conductivity also depends on the local temperature.As concerns commonly used materials, a good approximation of the the temperature dependent thermal conductivity is given as follows (mentioned in [27]):

$$k(T) = k(T_0)\Big(\frac{T}{T_0}\Big)^{-\alpha 1} \tag{2.7}$$

The value of T_0 is generally the room temperature (300K).This is in particular valid for

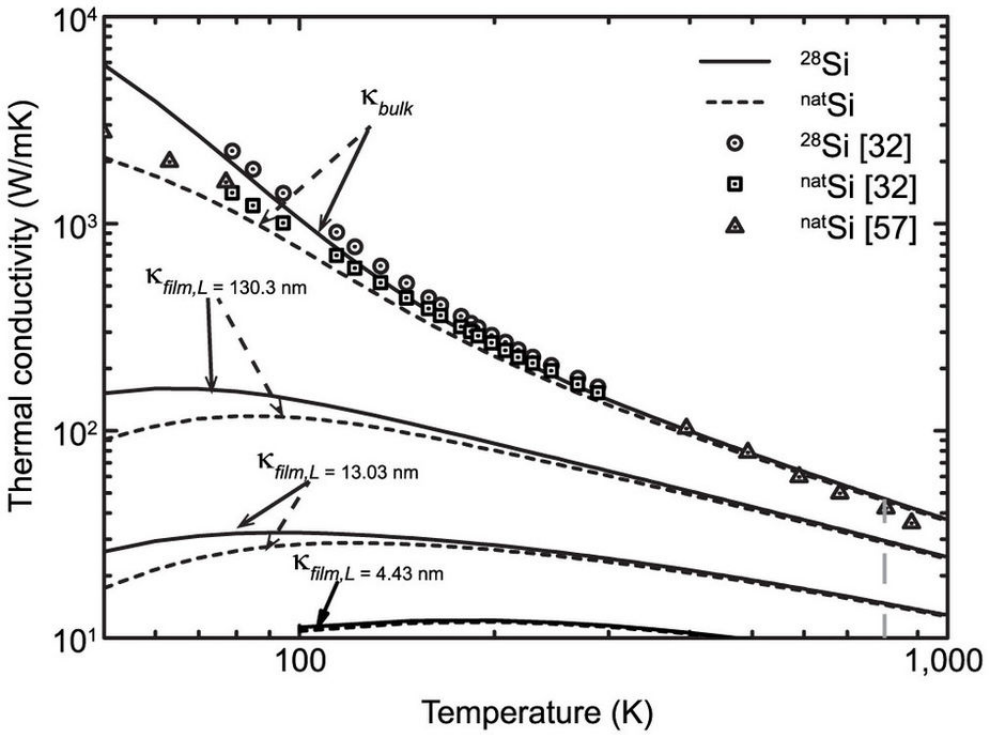

Figure 2.6: Variation of thermal conductivity (k) with temperature for different thicknesses ([28])

Film thickness/height (nm)	Thermal conductivity $k(W/mK)$	Temp. coefficient (α)
220	97	-0.7684
130	78	-0.7684
80	62.4	-0.7684
50	48.19	-0.4725
20	26.69	-0.4725

Table 2.2: Thermal conductivity (k) and associated temperature coefficient ($\alpha 1$) for different film thicknesses

Silicon and the value of $\alpha 1$ for bulk silicon is 1.65. Just like the thermal conductivity of Si changes with film thickness, so too does the temperature coefficient $\alpha 1$ ([28]). The coefficient $\alpha 1$ decreases with a decrease in film thickness i.e the fall in thermal conductivity with temperature is lesser for smaller thicknesses. This can be observed from the plot in figure 2.6 which was taken from [28]. The thermal conductivity decreases with film thickness because at lower thicknesses, phonon scattering increases. The thermal conductivity also decreases with temperature(T) due to the increased inter-phonon scattering at higher temperatures. Values for the thermal conductivity for different temperatures were again obtained using the 'WebPlotDigitizer' and the values obtained were fitted with the equation in 2.7. The plots were fitted using MATLAB and the fits were found to be very good having adjusted R-squared values greater than 0.99. The table 2.2 lists the values of the thermal conductivities at room temperature and the temperature coefficients for the different values of film thickness. The temperature data was available only for the film thicknesses $13nm$ and $130nm$. The temperature coefficients for other thicknesses where taken based on how close the thicknesses were to the available data-points(i.e $130nm$ and $13nm$).

2.6 Results and Discussion

The simulations were executed based on the framework mentioned in 2.2.The simulation window for the DEVICE simulations was $20\mu m \times 5.1\mu m$ and the simulation window for for the MODE simulations was $7.2\mu m \times 4.2\mu m$.The geometries (CAD Model) for the simulations on both platforms were identical and the Silicon was defined as an index-perturbed material in MODE.The device parameters used in both the

Parameter	Value
$Waveguide - Dimensions$	$480nm \times 220nm$
$H(overclad - thickness)$	$900nm$
g	$300nm$
W_h	$900nm$
t_h	$50nm$
$Underclad - thickness$	$2\mu m$

Table 2.3: Device parameters chosen for Thermo-optic Simulation

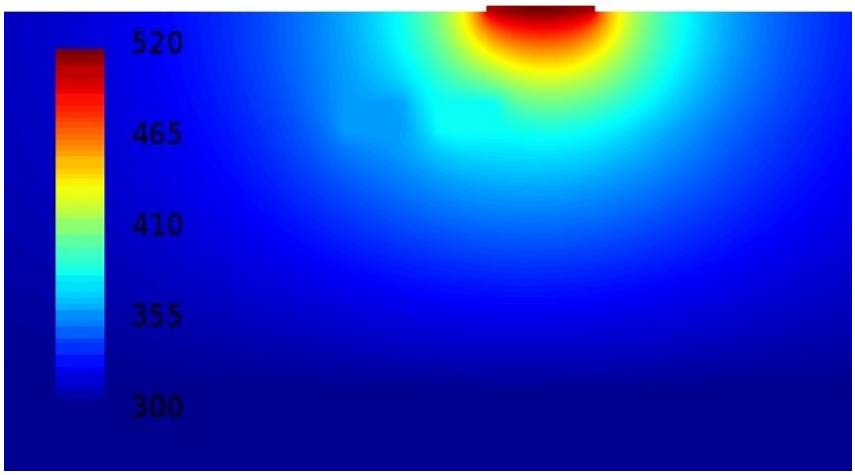

Figure 2.7: Temperature profile obtained from DEVICE for the design [$P_D = 20mW$,$d = 0.6\mu m$]

experimental study as well as our simulation are shown in the table 2.3.The thermal profile obtained from DEVICE with $P_D = 20mW$ and $d = 0.6\mu m$ is also shown in figure 2.7 for reference.

The simulations were executed using both phonon scattering affected thermal conductivity as well as the bulk thermal conductivity values of Silicon. The results of the thermo-optic simulations are shown in figure 2.8(a). We find that including the Phonon scattering effects slightly improve the tuning, but not by much. This is expected since the area of cross section of silicon is very small ($480nm \times 220nm$) and this means that the effects of Phonon scattering though significant in the absolute sense do not have a significant effect on the design performance. The corresponding experimental results obtained in the the paper are also shown for reference in figure 2.8(b). The simulations follow the trends mentioned in the paper, specifically the observation that $d = 0.6\mu m$ results in the maximum tuning.The simulations agree very well with the experimental study at $d = 0.6\mu m$. At $P_D = 30mW$, the experimental value was around 0.5 whereas

our simulation gave a value of 0.4675 (including phonon-effects). This essentially also means that the Tunability (Γ) values are also very similar, with the simulated value being $24.143W^{-}1$ and the actual value around $19.132W^{-}1$ (evaluated with plot digitizer).

The discrepancies arise though at $d = -0.3\mu m$ and $d = 0\mu m$. We hypothesize that these results can be attributed to 'edge effects' or heating in the areas outside the region under our study i.e regions outside the coupling length. At these values of d, the gradients in Coupling length region are less since the heater moves toward a symmetric position. If the heater is placed exactly in between the waveguides, in theory, the tunability is supposed to be zero. This is very close to the case where ($d = -0.3\mu m$), where the heater is placed just $90nm$ away from the point of complete symmetry. This means that in theory ,the tunability must be negligible (as shown in our simulation results), though a significant tunability is observed in the experimental results.

The absolute temperatures in the coupling regions and the bend regions increase significantly when d decreases. This essentially means that the heating at the bend region or farther areas will gain the upper hand. We hypothesize that it is the heating in these regions that cause the mismatch in the experimental results and simulation results. Since the K is evaluated by using a Ring resonator based approach, significant rise in the temperatures at the bend region should in principle change the transmission characteristics. This is what was termed as the 'edge effect'.Systematic three dimensional simulations are required to understand these effects.Overall, in the region of interest ($d = 0.6\mu m$), the simulation and experimental studies agreed well. This provides a basis to evaluate other designs.

The advantage of this design lies in the optical insulation that the over-clad provides for the guided modes from the metallic heater. This design is lossless and since the thermal conductivity of the over-clad is very small ($1W/mk$), effectively confines the heat in the over-clad region to create a temperature difference between the two waveguides constituting the directional coupler.The areas of improvement for this design include faster response times and a greater temperature difference between the waveguides. The response time (τ_{resp})is relatively higher due to greater area/volume to be heated on account of the Oxide over-clad. The temperature difference, though significant can be improved through better design. These issues are addressed in the later designs.

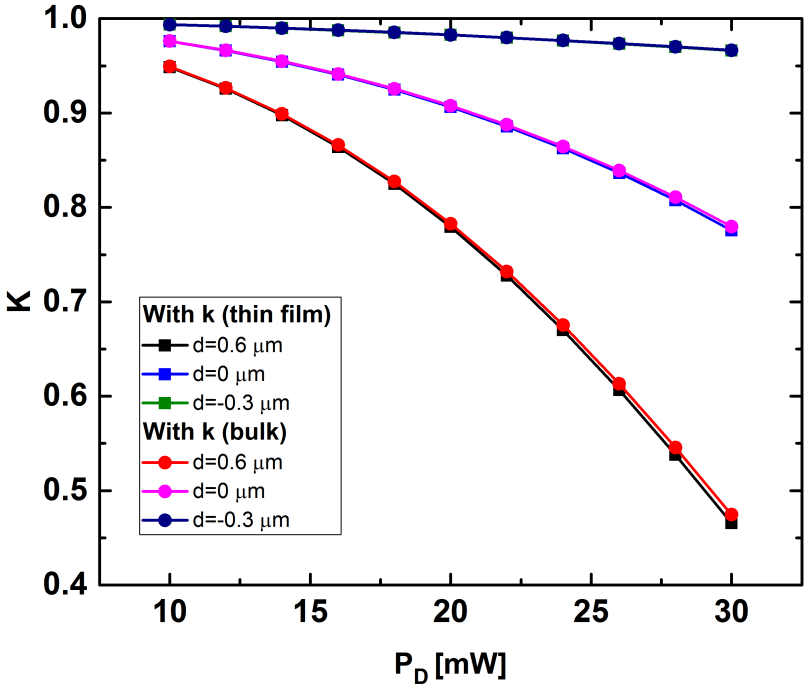

(a)

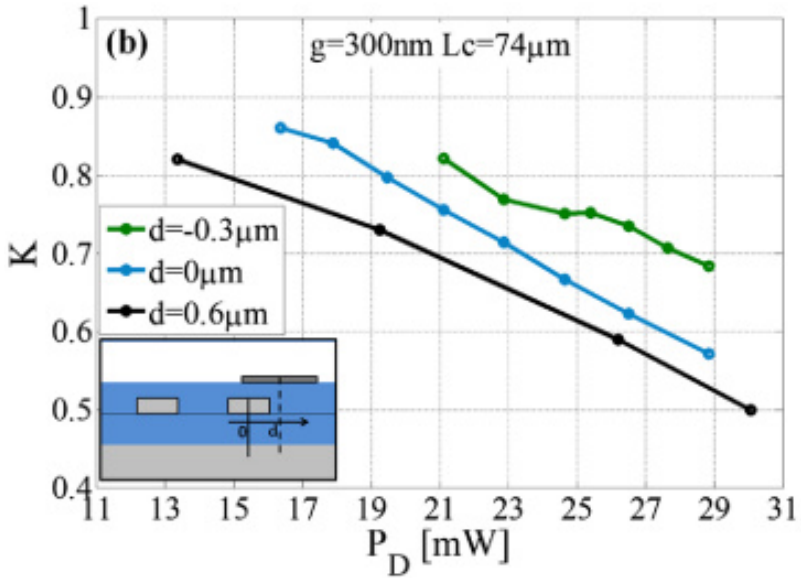

(b)

Figure 2.8: K vs power dissipated [P_D] obtained from (a) Simulation study (b) experimental study

CHAPTER 3

Tunable Directional Coupler with Heater placed parallel to waveguide

As seen in the previous chapter, a tunable directional coupler driven by a Transverse temperature gradient was proposed which had good Tunability [Γ]. A model was also proposed to evaluate the performance of the design through simulations. The results obtained from the model were found to be in close agreement with the experimental results at greater distances between the heater and the midpoint of the second waveguide especially at $d = 0.6\mu m$ which was the optimum distance for heater placement. Though the design performance is good, there exists a need for a design that is:

1. Easier to fabricate
2. Faster in its response to any input
3. Has a better performance with regards to Tunability (Γ)
4. Easier to integrate with devices designs or applications with no over-clad (Eg: Adjusting power fraction in Ring Resonator to attain critical coupling).

With this in mind, we have proposed a Tunable Directional coupler design with the heater placed in parallel (as shown in Fig 3.1), to make better use of the Transverse temperature gradient produced by the heat source. The only issue with this design though is the loss due to the presence of the heater material (metal) which is also considered during the evaluation and subsequent proposal of an optimal solution. As in the previous chapter, all the designs are evaluated for the fundamental TE mode and the operating wavelength is $1.55\mu m$. Also, Titanium (Ti) heaters are used in place of NiCr heaters in the previous case. Titanium is used as the material because of its high resistivity, high melting point and also because it has been integrated into device designs in our lab[29]. The material properties of Ti are as shown:

Materials	$\rho(\frac{Kg}{m^3})$	$C_p(\frac{J}{KgK})$	$k(\frac{W}{m^2K})$
Heater(Titanium)	4500	520	21.9

Table 3.1: Material properties of Titanium [30]

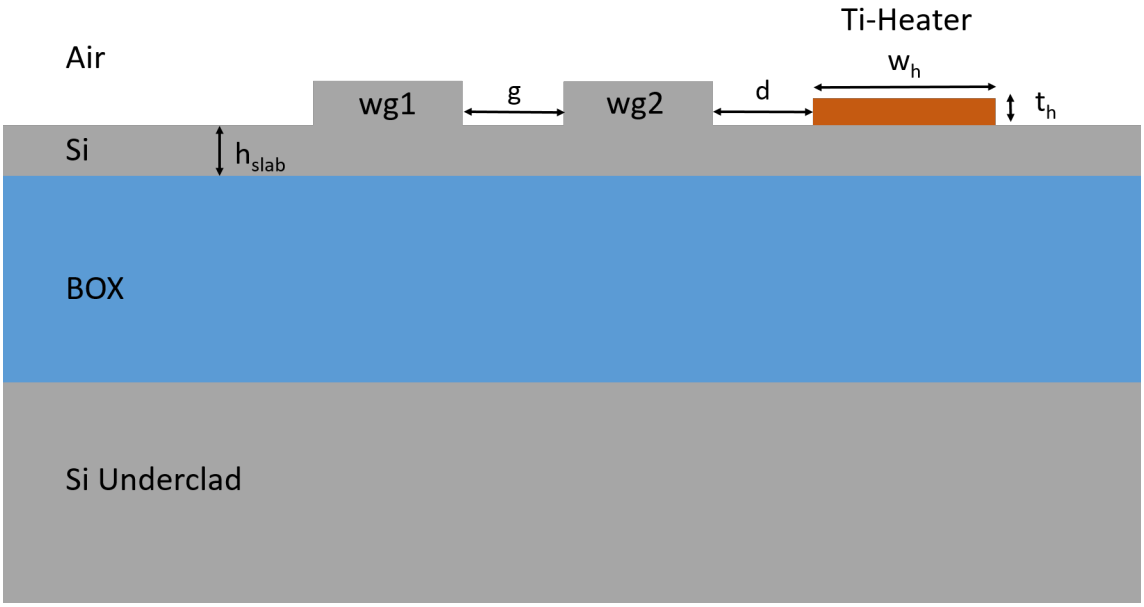

Figure 3.1: Schematic for the cross-section of the rib waveguide based TDC design (wg1 and wg2 are the rib waveguides)

3.1 Tunable directional Coupler without Over-clad

First, we evaluate the performance of the design where rib waveguides are used as the constituents of the directional coupler with the heater placed atop the slab region.An over-clad is not used in this design. This is shown in Figure 3.1 .The main motivation for this design is to design a TDC without the over-clad, with its corresponding advantages as mentioned above.

3.1.1 Waveguide and Directional Coupler design

The device layer thickness was taken to be $220nm$ and the waveguide/rib width was taken to $540nm$, in line with the already existing requirements and process flow in the lab. The slab height (h_{slab}) was chosen based on the figure shown in 3.2 .This figure was generated after studying the condition for single mode guidance through the simulations carried out in MODE solutions.The underlying condition for the propagation of any

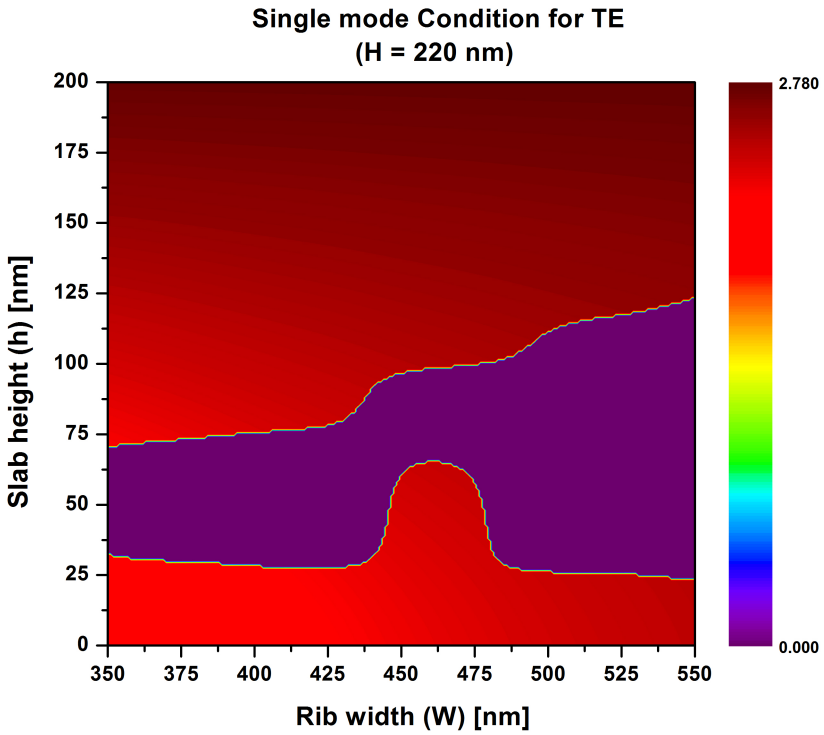

Figure 3.2: 2-D plot with different values of rib width and slab height to ascertain Single mode condition for TE (red- single mode guiding; purple-multi-mode guiding)

guided mode in the rib-waveguide is that the effective index of the guided mode must be greater than that of the slab mode for guidance.For exclusively single mode guidance, the first order mode must not be guided. This means that the effective index of the first order guided mode should be less than the corresponding slab effective index for single mode guidance. Essentially, the red region represents the area where only the fundamental TE mode is guided and the purple region represents the area where the waveguide guides multiple TE polarized modes.

Simulations were executed over a wide range of values for rib width and slab height.The corresponding results are shown in 3.2. We can see from the figure that there exists a cutoff height above which the waveguide guides only the TE fundamental mode. This is because, as the height of the slab increases,the effective index of the slab mode increases and at a certain height, exceeds the effective index of the first order TE mode. This is in line with the observations at the micron-scale.This figure however does not provide any data about the guidance of TM polarized modes.The behavior of the TM polarized modes in general and the TE polarized modes at very low slab

heights are complex and may involve conversion of a 'hybrid mode' from TE to TM or vice versa when the rib width/ slab height is changed.

At the sub-micron dimensions as used in this study, hybrid modes become an issue. A hybrid mode is a mode which cannot be completely termed as either a TE or a TM mode. A quantity called TE polarization fraction is used to distinguish or resolve the polarization of the mode. The TE polarization fraction for propagation along the z-direction is defined by :

$$TE - polarization fraction(\phi) = \frac{\int |E_x|^2 dxdy}{\int (|E_x|^2 + |E_y|^2) dxdy} \tag{3.1}$$

This basically gauges the strength of the dominant field component in a TE polarized mode (E_x) relative to the other components. The terms TE polarization fraction and polarization fraction are used interchangeably in this thesis. If the TE polarization fraction is 100, this means that the mode is completely TE in nature. If the TE polarization fraction is 0, this means that the mode is completely TM in nature. In reality, the acceptable values for purely TE modes vary from 90 to 100 and the the acceptable values for purely TM modes vary from 0 to 10. A hybrid mode is one that possesses a TE polarization fraction value not mentioned in the ranges above.
For hybrid modes, the polarization is resolved using the following conditions:

1. if $\phi > 50$, mode is TE polarized
2. if $\phi < 50$, mode is TM polarized

The TE polarized modes were studied in the figure 3.2. But for the TM polarized modes, simulations were done individually to ascertain the guidance of such modes.

A slab height of $130nm$ was chosen, such that only the fundamental TE mode (Fig 3.3(a)) was guided. A guided TM mode was also obtained with a polarization fraction of 22%. Whilst it was guided, the power confinement(eq 3.2) within the rib-waveguide cross-section was found to be 23.8409%.This is due to the spreading of the mode in the cladding as can be seen from figure 3.3(b). This is very less as compared to the confinement for the fundamental mode (70.8621%). The mode profiles for both modes can be seen in figure 3.3. The dominant Electric field components are shown in the

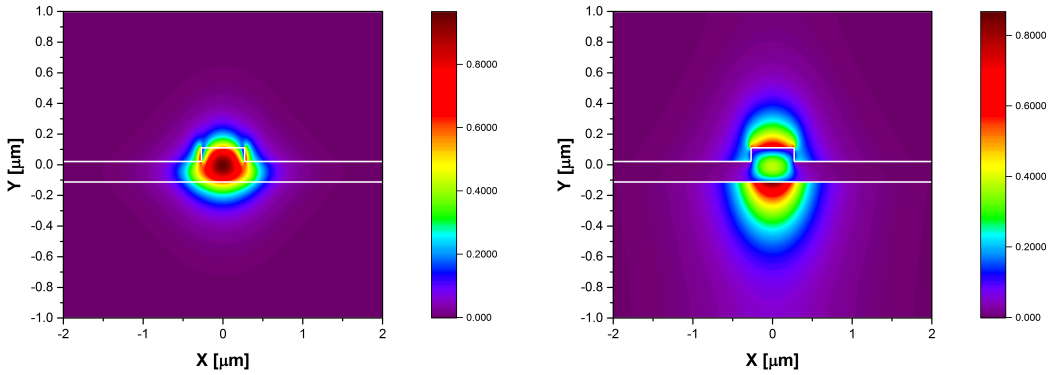

(a) (b)

Figure 3.3: Modal field strength (magnitude) profiles for (a) E_x of Fundamental TE mode (b) E_y of Fundamental TM mode ($h_{slab} = 130nm, rib - width = 540nm$)

figure i.e E_x for TE and E_y for TM. The power confinement fraction/percentage/factor mentioned above is defined as follows:

$$Confinement - factor(\sigma) = \frac{\int_{x_1}^{x_2}\int_{y_1}^{y_2}(\vec{E}\times\vec{H})_z dxdy}{\int_{-\infty}^{\infty}\int_{-\infty}^{\infty}(\vec{E}\times\vec{H})_z dxdy} \tag{3.2}$$

where x_1 and x_2 represent the x limits of the region where the power confinement is to be computed and y_1 and y_2 represent the corresponding y limits where the power confinement is to be computed.The gap between the waveguides (g) is taken as $300nm$ which is the same value of gap used for the overclad case.

3.1.2 Results and Discussion

The Thermo-optic simulations were carried out for the design using the formulation as mentioned in 2.2.The parameters used during the simulation are given in the table 3.2. The thermo-optic simulations were carried for different values of d (distance between heater and the second waveguide). The thermal profile obtained from DEVICE with $P_d = 20mW$ and $d = 0.6\mu m$ is also shown in figure 3.4 for reference.

From the $K - P_D$ plots as shown in Fig 3.5,first we see that as the distance d increases,the tunability decreases. This is because the temperature gradient decreases as the heater is moved away from the DC. We also infer that the device performance overall

Parameter	Value
$Ribwaveguide - Dimensions$	$540nm \times 220nm$
h_{slab}	$130nm$
g	$300nm$
W_h	$900nm$
t_h	$50nm$
t_{BOX}	$2\mu m$

Table 3.2: Device parameters chosen for Thermo-optic Simulation

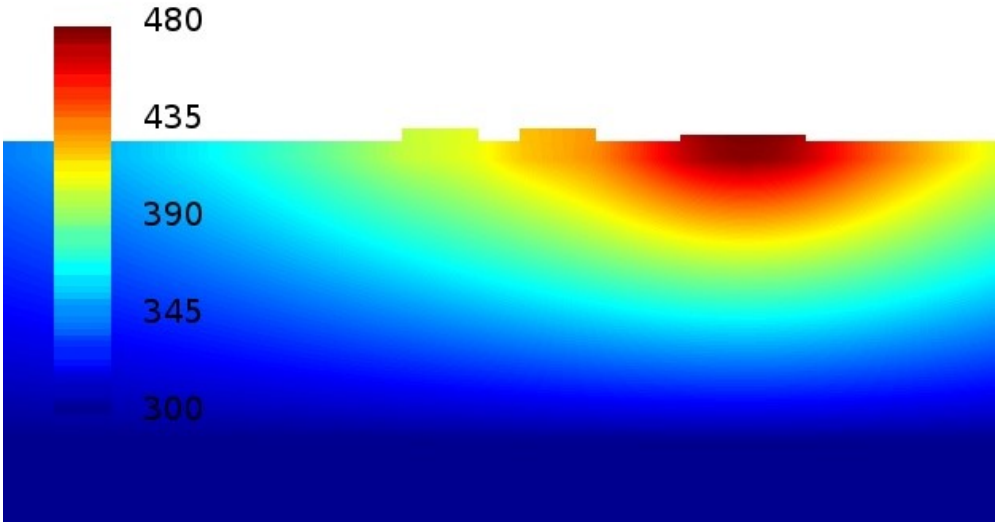

Figure 3.4: Temperature profile obtained from DEVICE for the proposed design [$P_D = 20mW$,$d = 0.6\mu m$]

(for all values of d) is very poor in terms of Tunability (Γ). K falls only to around 0.9 even when $P_D = 30mW$ is applied.This is principally because of the fact that Silicon is an extremely good conductor of Heat (k is very high), and the presence of Silicon in between the waveguides enables a very good amount of heat transfer between the waveguides, thus reducing the temperature difference/gradient between the waveguides. Essentially, at steady state:

$$Q = -\nabla \cdot (k \nabla T) \tag{3.3}$$

So, qualitatively, if k is higher, the gradient is lesser and if k is lower, this implies a greater temperature gradient.This essentially implies that the presence of Silicon in between the waveguides is a major impediment to obtaining a good design performance. This problem is addressed in the forthcoming proposals and is the key motivation for the differentially etched designs.

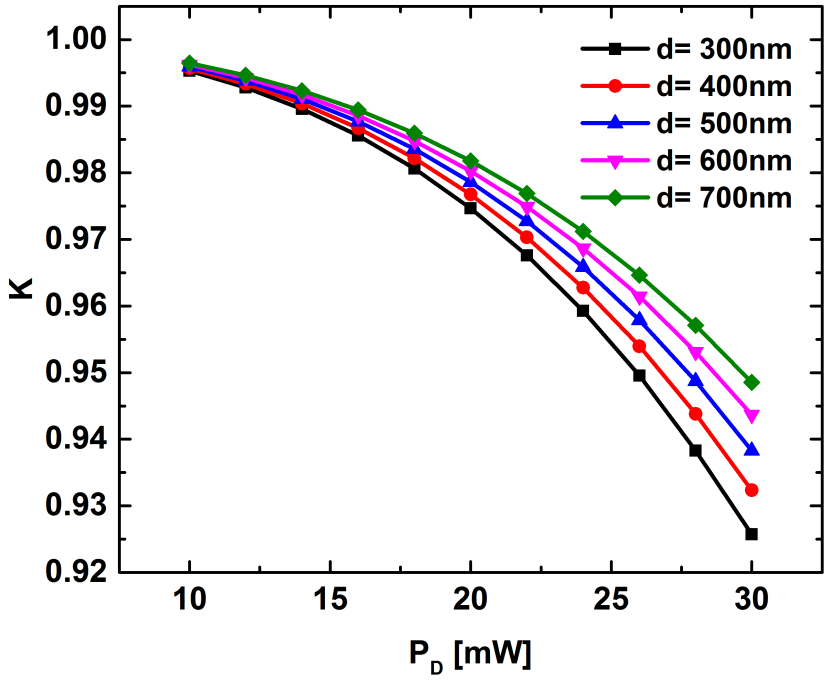

Figure 3.5: Variation of the coupled power fraction (K) with power dissipated (P_D) for different values of d (lateral distance between DC and Heater)

3.2 Differentially Etched Tunable Directional Coupler

In order to improve the performance of the Design where the heater is placed in parallel, a differentially etched design was chosen as shown in Figure 3.6. The slab region in between the waveguides is deeply etched comparative to the remaining slab region. This is done, because the lesser intermediate slab height implies a smaller path for heat to flow, essentially improving the thermal gradient between the two constituent waveguides. In addition to this, thermal conductivity decreases with the slab height and consequently strengthens the effect of increasing the temperature gradient/difference between the waveguides. The rib cross-section($540nm \times 220nm$),the height of the slab in remaining slab region ($h = 130nm$) and the distance between the waveguides ($g = 300nm$) were kept constant. The rib height in the intermediate region was decreased to approximately match the value of coupling length in the previous Chapter ($L_c = 74\mu m$). This was done to compare the effect of the heater on the Coupled power fraction (K) whilst maintaining a heat flux equal to that of the design mentioned in paper on TDC [8].

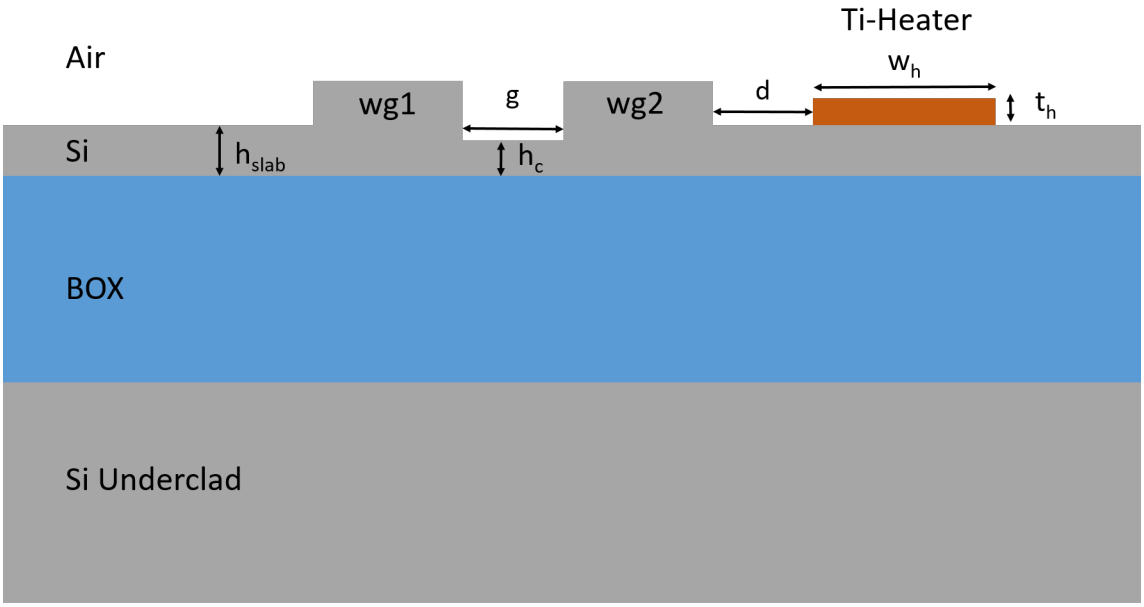

Figure 3.6: Schematic for the cross-section of the differentially etched TDC design

3.2.1 Waveguide and Directional Coupler Design

Single mode Verification

The waveguide cross-section was left unchanged principally to maintain the single mode condition in the constituent waveguides. The fundamental TE mode and the highest index TM mode or fundamental TM mode (Polarization fraction<50%) are found to be guided for a range of h_c values ($20nm - 80nm$).The remaining modes are lossy and the TE first order mode is found not to be guided.In the case where $h_c = 80nm$, similar to the previous case (fig 3.3(b)),we observe that the first TM mode is spread in the cladding and air region. The power confinement fraction 3.2 i.e the percentage of power passing through a given cross-section was computed for the rib cross-section and found out to be 15.091% (Polarization fraction= 47%),while the power confinement fraction for fundamental TE mode was 72.1652. The mode profile for the fundamental TE mode has also been shown in Fig 3.7.

For the TM mode, the E_x was also found to be lossy.Since, the polarization fraction is 47, a significant portion of the power is propagated through E_x.Thus the lowest order TM mode can be ignored. This verifies the fact that the single waveguide still guides only a single TE mode and can be effectively used for TE polarization based directional

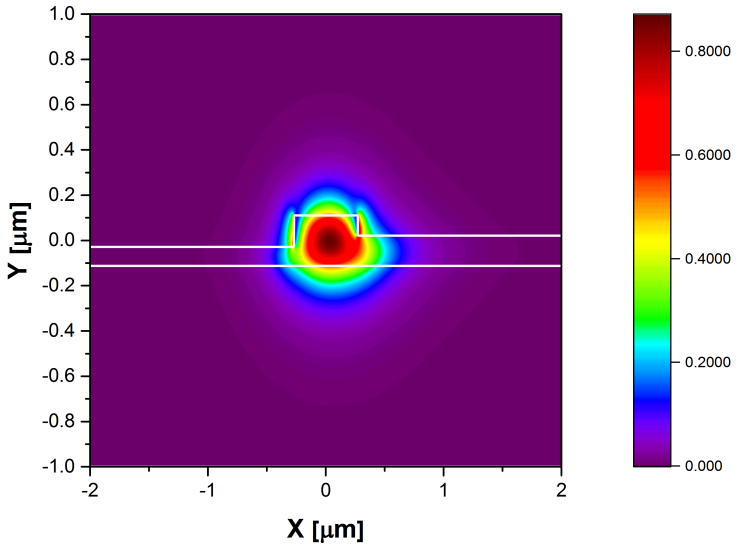

Figure 3.7: Modal field strength (magnitude) profile for E_x of Fundamental TE mode

coupler designs.

Optimization of the slab height in the intermediate region (d)

The slab height in the central region (h_c) is another important parameter of interest simply because it determines the coupling length (L_c), given that the distance between the waveguides (g) is constant at $300nm$. We choose to maintain the coupling Length ($L_c \approx 74\mu m$) to be equal to that chosen in the design mentioned in the paper [8], to obtain a better comparison in terms of performance. Keeping L_c constant ensures that, the heat power flux in the cross-section is kept constant (Heat power flux $[Q_f] = P_d/L_c$). Keeping the heat power flux constant, removes the Source as a performance parameter, especially since the heater cross-section has also been left unchanged. A parametric sweep was run on MODE solutions with h_c as the parameter and the graph above was obtained. As shown in the figure 3.8, as h_c increases, the coupling length decreases. This is because a greater height in the slab region implies better coupling between the modes, which in turn leads to a shorter coupling length. The exponential trend is also because the coupling is due to the interaction of tails which decay exponentially [22], and generally any trend that involves the interaction of these said exponential tails is exponential by itself.The value of h_c which resulted in a coupling length close to $74\mu m$ was found to be $80nm$ and the corresponding L_c was found to be $79.7978\mu m$.

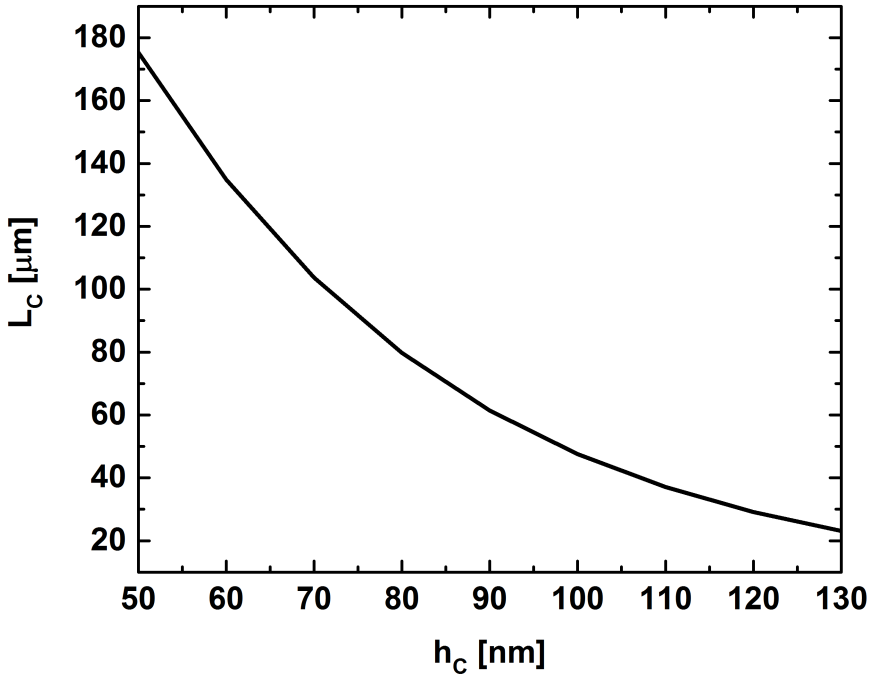

Figure 3.8: Variation of Coupling Length (L_c) with the height of the rib in the central region (h_c)

3.2.2 Optimization of heater offset and Thermo-optic study

The previous section dealt with the waveguide and directional coupler design in the absence of the heater. The introduction of the heater introduces two effects:

1. Loss due to interaction with metallic material (Ti)
2. Variation in Coupled power Fraction (K) due to introduction of Transverse Temperature gradient.

Both the effects are studied in order to get a complete picture of the design from a simulation viewpoint.

Optimization of loss due to adjacency of Metallic heater

As mentioned earlier, one of the disadvantages of placing the heater in parallel with the Directional Coupler is that the design becomes lossy. This is because the tail region of the mode interacts with the metallic heater. Metals have negative permittivity (absorption) and this implies that any overlap of the metallic region with a mode will cause loss due absorption in the metal.The placement of the metal is found to introduce loss,

but does not affect the effective index in any significant way. This is because the heater only interacts with the tail whilst the major part of the mode area is unaffected. This also further backed by the fact that the effective index of the guided modes do change, but the magnitude of the change is of the order of 10^{-4} and that too only for the cases where the heater is very close to the Directional coupler region.

The effects of loss due to placement of heater is also considered by simulating the directional coupler response whilst placing the heater in parallel. Thermal effects were not considered since the aim of this study is to provide a benchmark or a certain optimal configuration such that the losses can be maintained below a certain threshold $(0.5dB)$[16].The total loss for the configuration is estimated as follows:

$$Loss_{tot} = 0.5(Loss_{sym} + Loss_{antisym}) \tag{3.4}$$

where $Loss_{sym}$ and $Loss_{antisym}$ are the losses obtained for the Symmetric mode and Antisymmetric modes respectively.The power is equally distributed between the symmetric and antisymmetric modes, specifically when the modes are coupled using the arrangement as shown in figure 1.3 or in general when the two waveguides are far apart during the initial stages. So, the loss or $Loss_{tot}$ is taken as the average of the losses of the two component modes.Now, we should note that the average of power losses actually overestimates the loss, since the actual loss is the average of losses in absolute terms and not in dB units, this is shown below. The average of the losses in dB units was preferred due to ease of computation and also because the actual loss would be much lesser than the threshold.

$$Power_{actual} = 0.5(e^{-2\alpha(sym)L} + e^{-2\alpha(antisym)L})$$

$$Power_{estimated} = 10^{0.5(\log(e^{-2\alpha(sym)L}) + \log(e^{-2\alpha(antisym)L}))} = e^{-\alpha(sym)L \times -\alpha(antisym)L}$$

$$\implies Power_{estimated} \leq Power_{actual}(AM - GM \quad inequality) \tag{3.5}$$

where $\alpha(antisym)$ and $\alpha(sym)$ are the loss exponents obtained from the imaginary part of the refractive index, and $Power_{estimated}$, $Power_{actual}$ are powers left in the DC as a fraction of the initial power injected after propagating through a length L. Here

'estimated' refers to the power computed using 3.4 and 'actual' refers to the actual theoretical loss obtained using the coefficients obtained from simulations. Since the actual power fraction is always greater than the estimated power fraction, the actual loss (in dB) will always be less than the estimated loss dB. So, the method used gives an upper bound for loss which ensures the actual value will be well below the loss threshold.

Also, predictably the loss in the antisymmetric mode is found to be higher than the symmetric mode. This is due to the fact that the antisymmetric mode is spread out toward the edges in terms of Field intensity compared to the symmetric mode where the field intensity is also found in the intermediate slab region, essentially concentrating field intensity/power more toward the center and away from the heater. This is shown in Figure 3.9, where, the E_x field amplitudes computed for both the modes are represented.

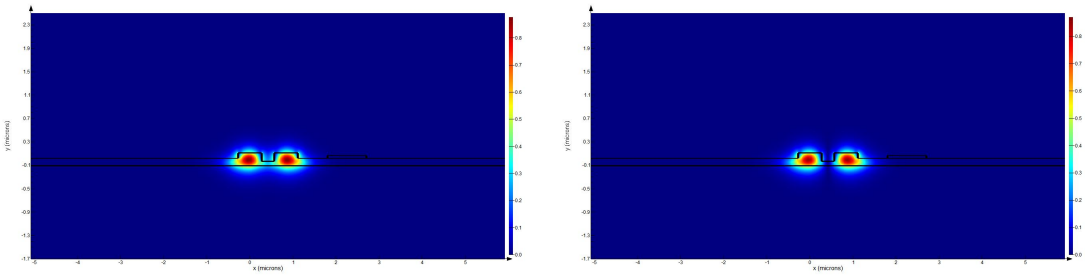

(a) (b)

Figure 3.9: E_x field profiles for both (a) Symmetric and (b) Anti-symmetric modes [$d = 0.7\mu m$]

Parametric sweeps were again undertaken where the heater position was varied by using the heater midpoint position as the parameter. The results obtained are shown in Figure 3.10 .The total loss across the coupling length as well as the loss per unit length have been shown. The Loss decreases as the metallic heater is placed farther away from the second waveguide and decreases exponentially. This is again due to the fact as the heater moves away, the interaction with the mode tail decreases and as mentioned before, any trend which involves the behavior of the exponentially decaying tails follows an exponential trend by itself. Finally, the optimal value for d was found to be $550nm$ with a corresponding loss of $0.4758dB$.

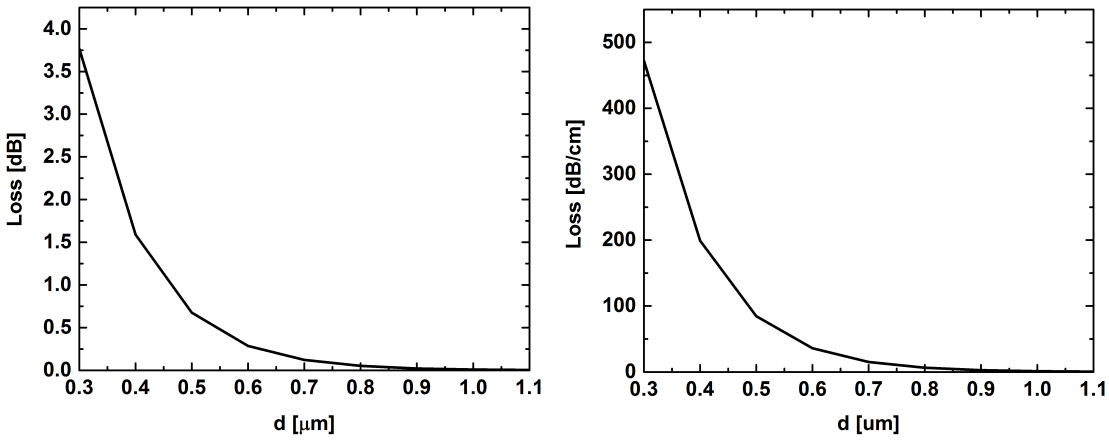

(a) (b)

Figure 3.10: Loss variation with the distance of the Metallic heater from the second waveguide [d] a) Loss across the Coupling length (dB) b) Loss per unit Length (dB/cm)

3.2.3 Thermo-optic response of the Differentially etched Tunable Directional Coupler design

After obtaining the optimized parameters as shown in table 3.3, thermo-optic simulation is executed based on the formulation as mentioned in 2.2.The values of Thermal-conductivity used are also mentioned in Table. Simulation windows of sizes are used in MODE solutions and DEVICE respectively. Both the simulations are carried out in the cross-section at the origin ($z = 0$)

The plot between Coupled Power Fraction (K) and Power Dissipated (P_D) as shown in figure 3.11 reveals that though the tunability has improved relative to the previous design ($K[diffetched, d = 550nm] < K[diffetched, d = 500nm]; P_D = 30mW$), it is still very poor as compared to the original design proposed in [8]. The slight improvement is because the path in terms of area has been decreased for thermal conduction between the waveguides and also because the thermal conductivity for the intermediate slab region is also lesser due to Phonon-limited value of Thermal conductivity. The overall performance of the device is poor because even with Si having lower thermal conductivity ($k_{300K}^{80nm} = 62W/mK$), it is still orders of magnitude higher than that of BOX ($k = 1W/mK$). Thus the persisting higher conductivity of Si still severely limits the performance of the device. Increasing the height of the slab also is a bad idea, since this will increase the losses since a greater portion of the mode area will reside in the

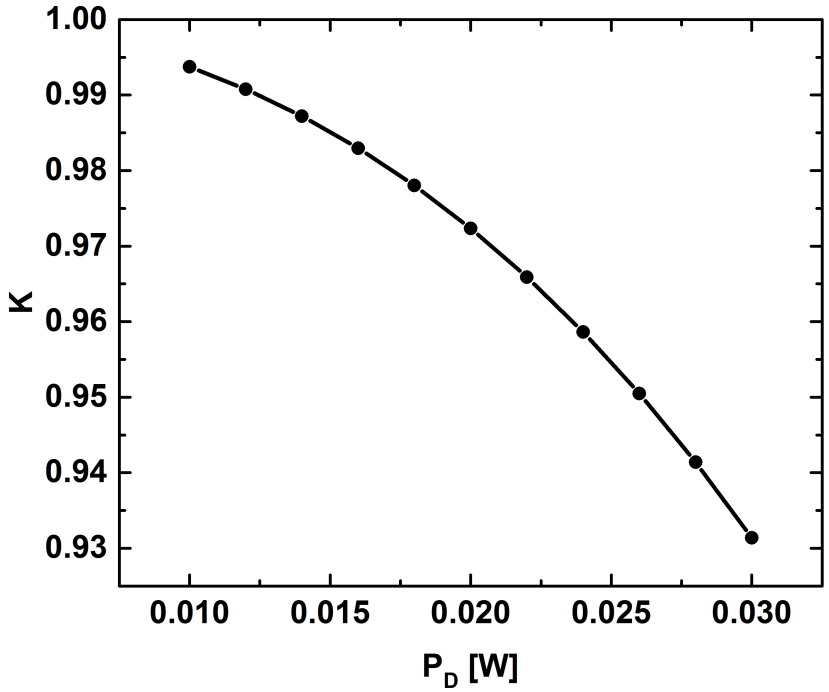

Figure 3.11: Variation of K with power dissipated (P_D) for the differentially etched design

slab region.

Figure 3.12 also shows the variation of the difference between the average temperatures of the waveguide and lateral offset of the heater (d). The average temperature difference was obtained by running a parametric sweep on COMSOL. COMSOL is used here because the vast array of post-processing options it possesses. Both COMSOL and DEVICE are found to produce the same temperature profiles with computationally insignificant differences. So, we establish that with regards to Thermal studies, COMSOL and DEVICE can be used interchangeably.From fig 3.12 we observe that as the

Parameter	Value
$Waveguide - Dimensions$	$540nm \times 220nm$
h_{slab}	$130nm$
h_c	$80nm$
g	$300nm$
d	$550nm$
W_h	$900nm$
t_h	$50nm$
t_{BOX}	$2\mu m$

Table 3.3: Device parameters chosen for thermo-optic Simulation of the differentially etched design

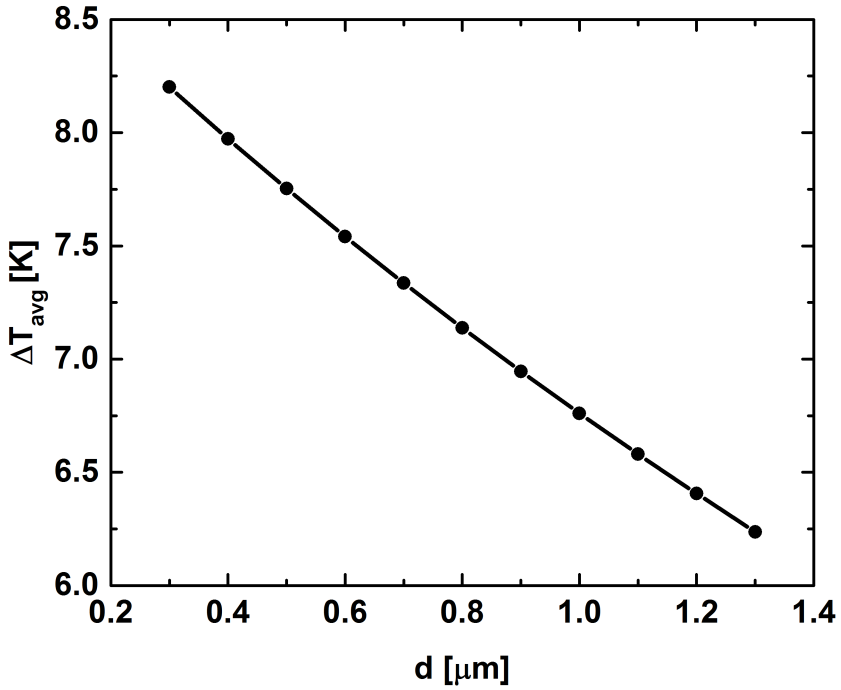

Figure 3.12: Variation of ΔT_{avg} or the difference between the average temperatures of waveguide2 and waveguide1 with power dissipated(P_D) for the differentially etched design

offset d increases, the temperature difference or gradient (used interchangeably in this thesis) falls for the given configuration. This means that for the loss threshold of $0.5dB$, the device performance cannot be significantly better than that shown in Fig 3.12, since both decreasing d (losses increase) and increasing d (lesser tuning) will both lead to unfavorable outcomes.So, the comments made with respect to poor performance of the device for $d = 550nm$ hold with regards to the overall device.

This paves the way forward for a new design where the intermediate region between the waveguides is completely etched. This optically coupled, but thermally decoupled design should have a much greater Tunability and this is discussed in the succeeding chapter.

CHAPTER 4

Optically coupled but Thermally decoupled Tunable Directional Coupler

The device designs discussed in the previous chapter provide a basis for a design with the heater placed in parallel to the Directional Coupler cross-section. Though, the designs discussed in Chapter 3 show a change in the coupled power fraction with the power dissipated (P_D), the tunabilities obtained were found to be exceedingly low. It is established that the thermal gradient is the driving force allowing for the tunability in the device in [8]. Hence, the poor performance is chalked down to the high thermal conductivity (k) of Silicon. It was also observed that though the tunability (Γ) is low, the differentially etched design shows a marginally better performance, confirming the hypothesis that thermal conductivity of Silicon is the limiting factor.To allow for the parallel placement of the heater whilst simultaneously allowing for a greater thermal gradient, the design shown in figure 4.1 is proposed. The central idea behind this design is to ensure that the waveguides are optically coupled but thermally decoupled (intermediate region completely etched). The thermal decoupling here essentially refers to the replacement of Silicon with air in the intermediate region, leading to thermal insulation between the waveguides. Though, some heat can pass through the underlying BOX, we posit that the removal of Silicon should have a significant effect on the average temperature difference (ΔT). It is this central idea leads to the apt name 'Optically coupled but Thermally decoupled TDC'.

We evaluate the designs for two slab heights (h_{slab}), 130 nm and 50 nm to also gain insights into the effect of varying slab height. The device characteristics and detailed study of the designs are discussed in the following sections.

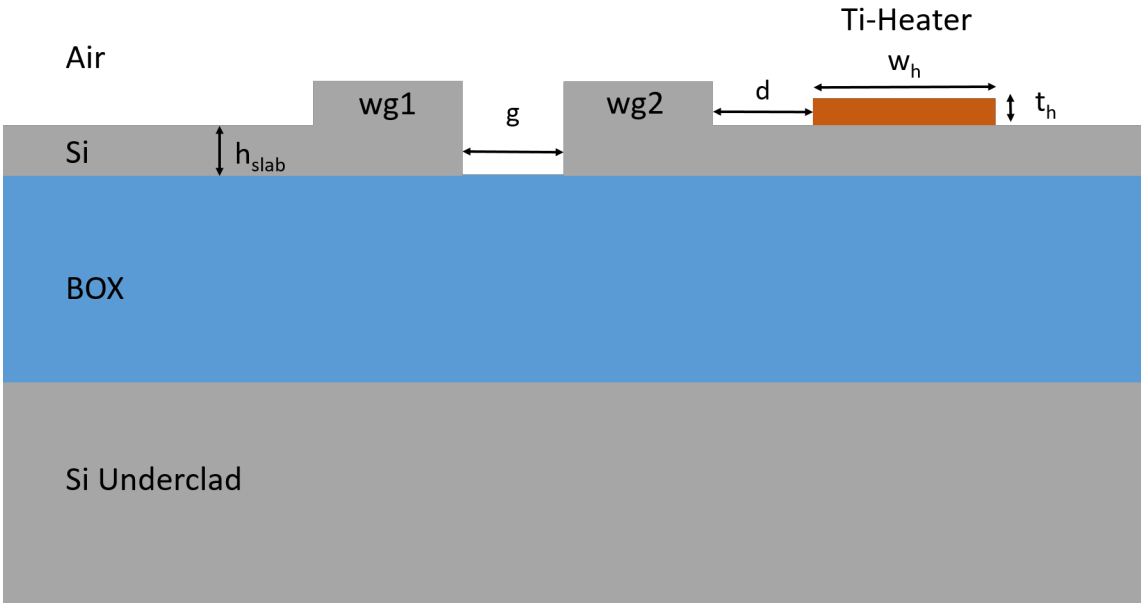

Figure 4.1: Schematic of the cross-section of the proposed Optically coupled but Thermally decoupled TDC

4.1 Waveguide design

The main motivation toward choosing a waveguide cross-section is making sure that the said cross-section is Single moded (TE and TM).The Modal analyses, the corresponding results and their implications on the rib waveguide design for the two slab heights considered are discussed below:

Case 1: Slab height= 130 nm

For the case where $h_{slab} = 130nm$ in the design proposed, the modes are found to be shifted more toward the slab region and away from rib (refer figures 4.2(a) and 4.2(b)), as compared to the symmetrically etched case.This is a big issue, since the coupling becomes significantly weaker. For, the same rib width of 540 nm, maintained from earlier, it was found that the gap (g) required to set the coupling length equal to $74\mu m$ was around $83nm$, ($< 100nm$) which is very difficult to fabricate. So in order to increase coupling, the rib width was decreased. This was done since, lesser width implies lesser refractive index (lesser confinement) and this means greater coupling between the two waveguides. Thus, the rib width was set to 450 nm to ensure that a gap

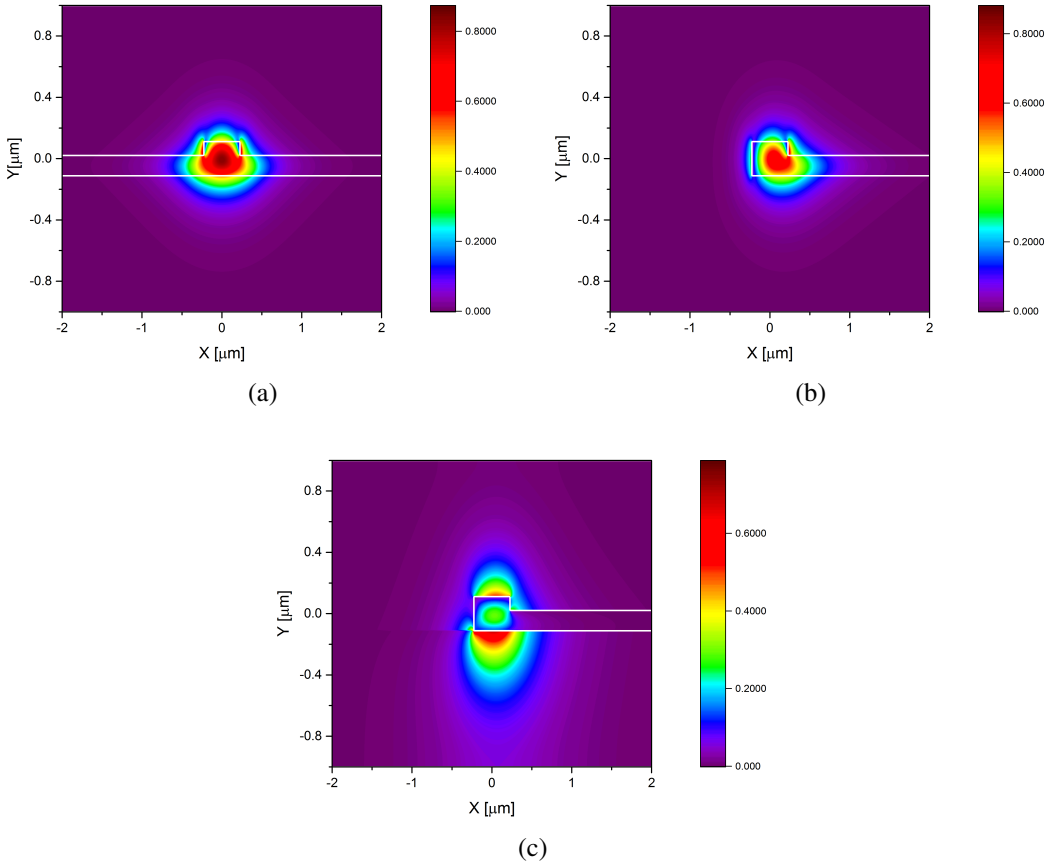

Figure 4.2: Modal field strength (magnitude) profiles for (a) E_x of Fundamental TE mode (symmetrically etched) (b) E_x of Fundamental TE mode (asymmetrically etched) (c) E_y of First TM mode obtained (fundamental TM) [$h_{slab} = 130nm$ and rib width=$450nm$]

greater than 100nm is required to set a coupling length of $74\mu m$.

It must be noted that the waveguides were exclusively single mode guiding for all the dimensions mentioned above. The mode profiles for the fundamental TE mode and the first TM mode obtained are shown in figures 4.2(b) and 4.2(c) respectively.The power confinement fraction (computed over waveguide cross-section [$0.22\mu m \times 0.45\mu m$]) for the TM mode was found to be 20.1623% which is much lesser than the confinement fraction for the fundamental TE mode (60.5976%-power also present in slab region). This is because the first TM mode is not confined properly, since a good portion of the field intensity is spread into BOX (Fig:4.2(c)). The H-components (magnetic field intensity) are also found to be lossy.All these observations essentially mean that though the TM mode is obtained theoretically, in practice such a mode cannot be excited/propagated effectively. So, it can be concluded that only the fundamental TE

mode can be guided effectively.

Case 2 : Slab height= 50 nm

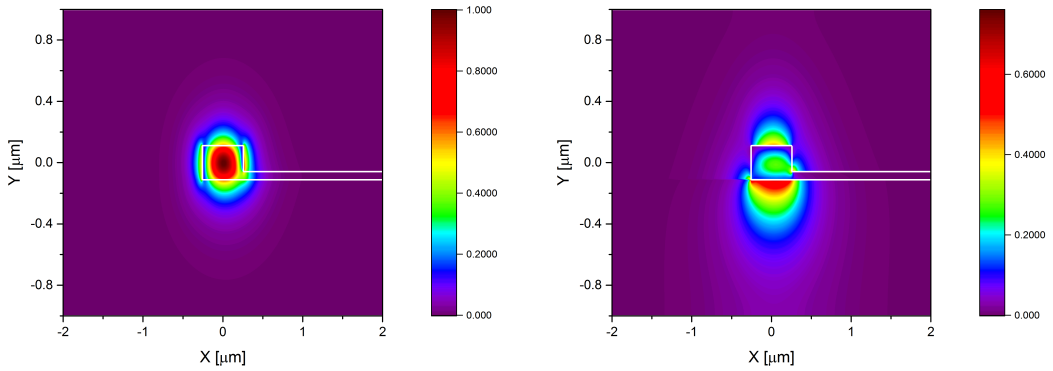

(a) (b)

Figure 4.3: Modal field strength (magnitude) profiles for (a) E_x of Fundamental TE mode (b) E_y of First TM mode obtained (fundamental TM) [$h_{slab} = 50nm$ and rib width=$510nm$]

For the case where $h_{slab} = 50nm$, we find that the number of modes that are guided depends on the dimensions. Since the slab height is lesser, the mode will be more confined in the rib region and consequently there will be more coupling between the modes in the intermediate region as compared to the previous case($h_{slab} = 130nm$). So, the design objective is different and involves only ensuring single mode guidance. The modal properties are not similar to that of the symmetrically etched case and the introduction of complete etching on one side in the sub-micron design considered presents the additional issue of hybrid modes.We would like to maintain the cross-section as similar as possible to that of the previous designs to maintain consistency. For rib widths around $700nm$, first order TE modes are found to be guided, whilst for lower rib widths [$450nm$-$560nm$] only two modes are guided. These modes are the fundamental mode and a second mode which is predominantly TM ($Polarization \quad fraction < 50\%$), but hybrid with Polarization fractions reaching values as high as 43% (560 nm) or even 53% (450 nm). The value of rib width was taken such that the polarization fraction was minimized. The value of rib width was found to be $510nm$ and corresponding polarization fraction was found to be 38%. The power confinement fraction for the TM mode was found to be 30.913%, whilst the power confinement fraction fraction for the

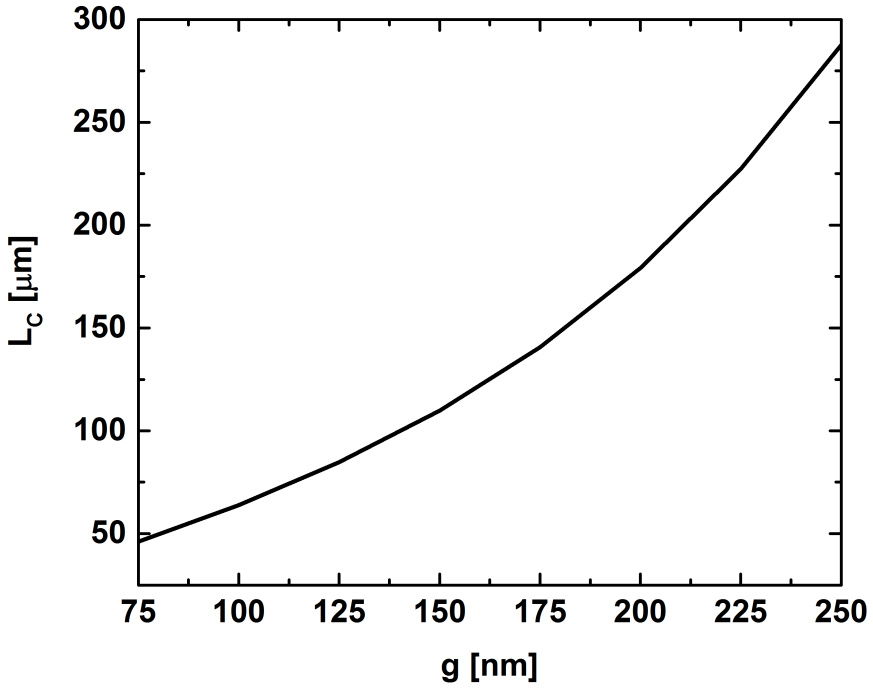

Figure 4.4: Variation of the Coupling Length (L_c) with the distance between the waveguides (g) for the case where slab height (h_{slab})=$130nm$

fundamental TE mode was found to be 79.721%. The confinements are higher, since the slab height is lesser i.e a lesser slab height implies a lesser cladding effective index (slab side) and consequently more confinement in the rib region since the refractive index contrast is more. Though the confinement is higher for the TM mode, it is not sufficient. The mode profiles obtained for the TE and TM modes are shown in figures 4.3(a) and 4.3(b). The dominant Electric field components have been plotted in both cases. We can observe that the TE mode is confined well and the TM mode is spread out into the cladding. This explains the power confinement values obtained. The lower confinement for the TM mode means that it cannot be guided effectively in practice.

4.2 Directional Coupler Design

Case 1 : Slab height= 130 nm

In order to maintain the coupling length (L_c) at $74\mu m$, a gap variation study is done.The coupling length is maintained so as to get a better comparison with the design with overclad as mentioned before 3.2.1.Here, instead of varying the etch depth in the middle,

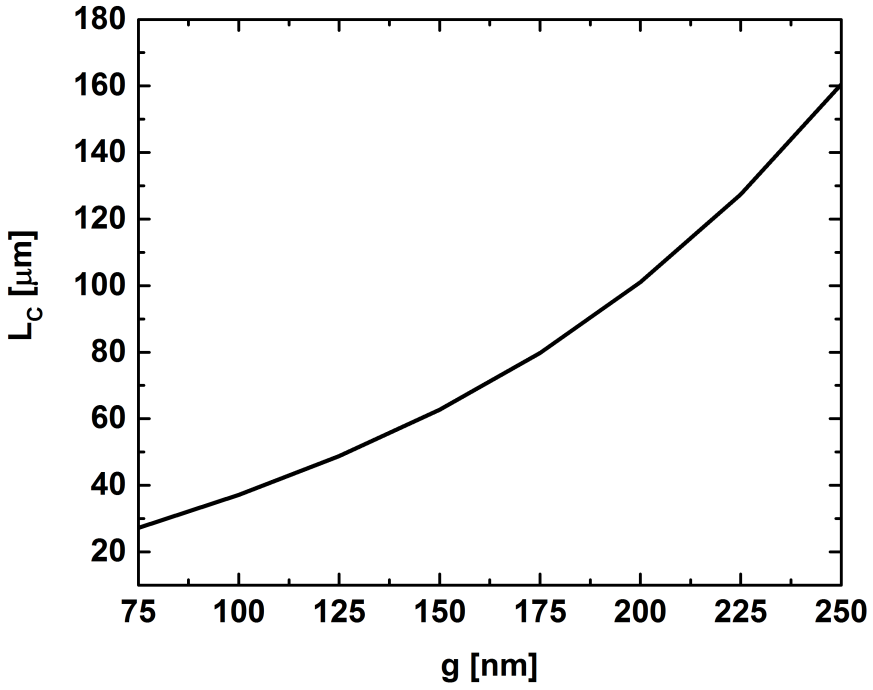

Figure 4.5: Variation of the Coupling Length (L_c) with the distance between the waveguides (g) for the case where slab height (h_{slab}=$50nm$)

the gap between the two rib waveguides is varied. A parametric sweep is run on MODE solutions with g as the parameter and the results obtained are shown in figure 4.4. The coupling length increases when the gap increases. This is because, the coupling length depends on the interaction of the mode tails of the guided modes in the independent waveguides. As the gap increases, the modal interaction between the two modes decreases (coupling decreases) and consequently L_c increases. The exponential nature of the plot can again be explained by the interaction of the exponentially decreasing tails. A finer sweep is run to find the value of gap which gives a coupling length closest to $74\mu m$. The value of gap(g) is found to be $113nm$, with the corresponding coupling length having a value of $73.8873\mu m$.

Case 2 : Slab height= 50 nm

Following the methodology adopted in the previous case, a parametric sweep with g as the parameter is run on MODE solutions to find the value of gap that gives L_c closest to $74um$. The plot obtained as a result of the parametric sweep is shown in figure 4.5. A finer sweep is run and the value of g is estimated to be $168nm$. The corresponding

L_c is found to be $74.2858\mu m$.

4.3 Loss optimization

Case 1 : Slab height= 130 nm

As mentioned in the previous chapter (3.2.2), the heater is placed in parallel to directional coupler region and its distance from the second waveguide is varied to estimate the heater position where the loss is lesser than a certain threshold ($0.5dB$). The total loss is estimated as the average of the loss in the symmetric and antisymmetric modes (equations 3.4,3.5).A parametric sweep is executed on MODE solutions with d (refer 4.1) as the parameter. The resulting plot is shown in the figure 4.6. We observe that the loss reduces when the heater is placed farther away from the DC region. This can again be attributed to the interaction of the modal tail with the metallic heater. As the heater moves farther away, the interaction between the mode tail and the metal decreases and consequently the loss decreases. The exponential nature of the plot can also be attributed to the mode tail-metal interaction.The optimal value of d was estimated to be $800nm$ where the loss was evaluated to be $0.4114dB$.

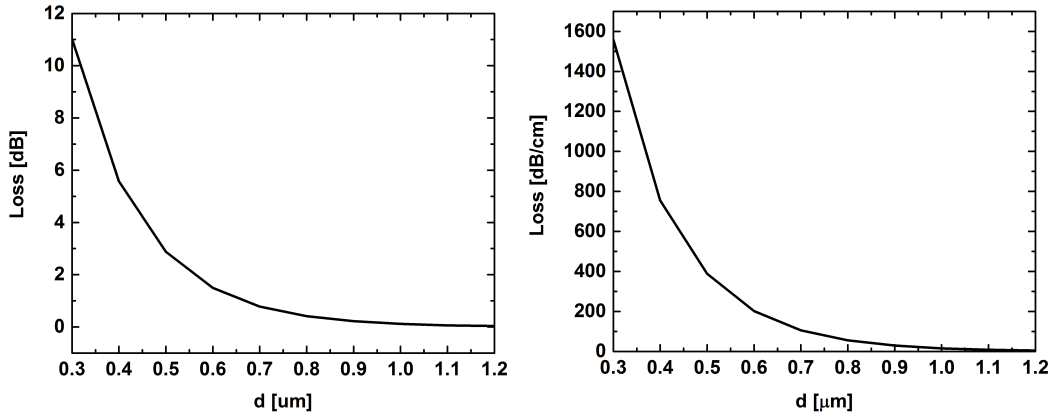

(a) (b)

Figure 4.6: Case 1: Loss variation with the distance of the Metallic heater from the second waveguide [d] a) Loss across the Coupling length (dB) b) Loss per unit Length (dB/cm)

Case 2 : Slab height= 50 nm

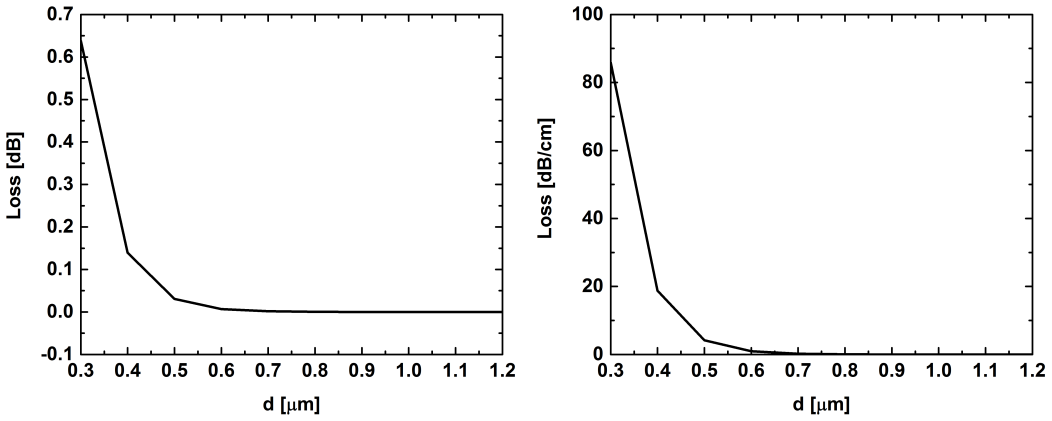

(a) (b)

Figure 4.7: Case 2: Loss variation with the distance of the Metallic heater from the second waveguide [d] a) Loss across the Coupling length (dB) b) Loss per unit Length (dB/cm)

As in the previous case, the distance (d) was varied and the effect on Loss was studied by running a parametric sweep on MODE solutions with d as the parameter. The plot obtained is shown in figure 4.7. Though the trend of loss decreasing with increasing d holds, we observe that the losses evaluated in Case 2 are an order of magnitude lesser than those of case 1. This can be attributed the tighter confinement of the mode in the rib region in case 2 as compared to case 1. The tighter confinement stems from the fact that as the slab height decreases, the effective cladding index decreases and more of the mode is confined in the rib/core. This can be understood by referring to the mode profiles in Figures 4.3(a) and 4.2(b) respectively. This effectively allows us to place the heater much closer to the DC region in case 2 rather than case 1.

A value of $400nm$ was taken for d with a corresponding loss of $0.13937dB$. The fact that this estimated value of loss is significantly lesser than $0.5dB$ though the heater is kept much closer points to the possibility of better device performance in case 2.

4.4 Thermo-optic Study

After completing the studies mentioned above, we get a set of optimized parameters to carry out our simulations with.In order to incorporate the effects of varying d on the

Parameter	Value
$Ribwaveguide - Dimensions$	$450nm \times 220nm$
h_{slab}	$130nm$
g	$113nm$
L_c	$73.8873\mu m$
d	$0.8\mu m, 1.2\mu m$
W_h	$900nm$
t_h	$50nm$
t_{BOX}	$2\mu m$

Table 4.1: Device parameters chosen for case 1 ($h_{slab} = 130nm$)

Parameter	Value
$Ribwaveguide - Dimensions$	$510nm \times 220nm$
h_{slab}	$50nm$
g	$168nm$
L_c	$74.2858\mu m$
d	$0.4\mu m, 0.6\mu m$
W_h	$900nm$
t_h	$50nm$
t_{BOX}	$2\mu m$

Table 4.2: Device parameters chosen for case 2 ($h_{slab} = 50nm$)

overall device performance, two values of d for each value of slab height have been considered (each resulting in a loss less than $0.5dB$. The consolidated list of parameter values used for each slab height can be found in the tables 4.1 and 4.5.

Using the parameter values mentioned in the tables and the material properties mentioned in tables 3.1 and 2.1, we carried out the thermo-optic simulations according to the formulation developed in 2.2. The simulation windows taken in DEVICE and MODE were $40\mu m \times 7.3\mu m$ and $28\mu m \times 4.2\mu m$ respectively. The simulation window for computing the n_{eff} of the individual waveguides were slightly varied, since mode sizes were much smaller. Specific importance was given to the mesh resolution and boundary placement to ensure physically viable solutions. The Phonon limited thickness dependence and the corresponding temperature dependence of Silicon thermal conductivity (k) are also considered in the simulation. The values are used according to the tables 4.1 for case1 and 4.5 for case 2. The results obtained are shown in figures 4.8(a) and 4.8(b).

The values of Tunabilities obtained for the different slab heights and values of d

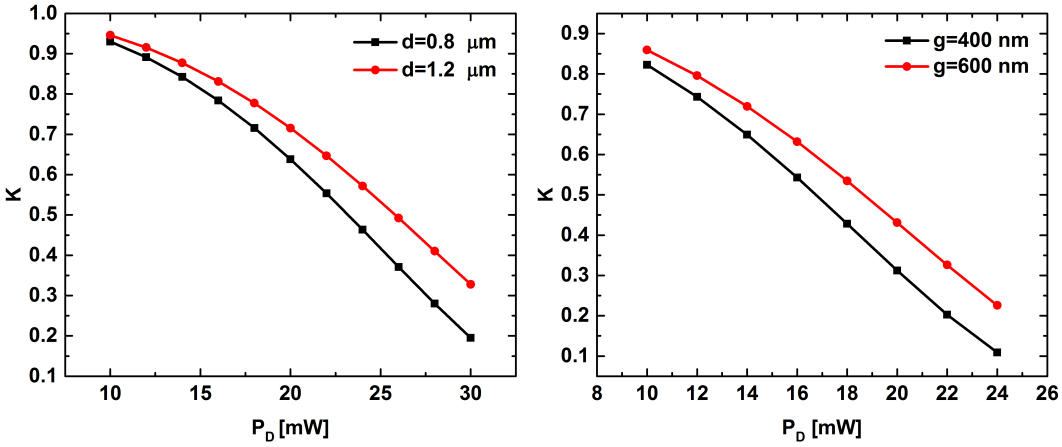

(a) (b)

Figure 4.8: K vs power dissipated (P_D) for (a)$h_{slab} = 130nm$ and (b)$h_{slab} = 50nm$ for different values of d

alongside the losses are consolidated and shown in table 4.3. We see that Tunability decreases as d increases. We also observe that the tunability (Γ) for case 2 ($h_{slab} = 50nm$) is significantly higher compared to case1.The factors that explain this include the closer placement of the heater to the DC region, greater gradient due to lesser heat flow and the greater gap between the waveguides in case 2. It is expected that the closer placement of the heater introduces a larger gradient. Concurrently, there is lesser heat flow in case 2 since the thermal conductivity decreases significantly with slab thickness, increasing the gradient. The greater gap (g) in case 2 ($168nm$) also ensures that the heat that passes through the BOX does not reach the first waveguide (wg1) effectively, thus increasing the gradient.The tunabilities obtained are also greater than the value obtained for the overclad design. The K values at the maximum powers dissipated are also lower. Specifically for the case 2, the maximum power dissipated is at $24mW$ rather than $30mW$ for the other cases, yet there is a significant drop in K. Thus laterally placed heater designs are proposed with better tunabilities and small losses.

Device specifications	$\Gamma[W^{-1}]$	$K[(P_D)^{max}]$	Loss(dB)
Overclad heater$(d = 0.6\mu m)$	24.1435	0.466	0
Proposed Design $[h_{slab} = 130nm : d = 0.8\mu m]$	36.1109	0.195	0.409
Proposed Design $[h_{slab} = 130nm : d = 1.2\mu m]$	29.7639	0.328	0.032
Proposed Design$[h_{slab} = 50nm : d = 0.4\mu m]$	50.9827	0.109	0.139
Proposed Design $[h_{slab} = 50nm : d = 0.6\mu m]$	45.2569	0.226	0.007

Table 4.3: Tunability (Γ), power fraction at the maximum P_D and associated losses estimated for selected device designs evaluated, Proposed Design is the Optically coupled Thermally decoupled design

4.5 Comparison of the Tuning mechanisms in the proposed designed with the design having overclad

Whilst K decreases with dissipated power(P_D) for both the newly proposed design and the previous design with over-clad, it is imperative to understand the mechanism of tuning and the differences in the mechanisms to get a better picture in terms of performance. To compare the designs we take two design specifications. For our proposed design, we take the case with $h_{slab} = 130nm$ and $d = 0.8\mu m$(Design 2) and for the case with overclad heater, we take the case where $d(offset) = 0.6\mu m$(Design 1) We have taken the optimal specifications for both cases to understand the tuning mechanism better. To do so, the Coupled Power equation as written in 2.1 is split into 2 constituents:

$$K_\kappa = \frac{|\kappa|^2}{S^2} \tag{4.1}$$

$$K_{\sin} = (\sin(SL_c))^2 \tag{4.2}$$

This is done in order to separate the Tuning action into two distinct components.The component in equation 4.1 (K_κ) captures the effect of the relative variation of $kappa$ with respect to S, which is basically how κ/S varies with power. The component in equation 4.2 captures the effect of S alone since L_c is constant.

In Figure 4.9(a), we see the K_κ of both the designs placed side by side for the same range of power.We observe that both the K_κ fall by roughly the same amount i.e their behavior is not that different. We see that $K_{\sin}$ is significantly different for the designs with design 1 having a much larger fall as compared to design 2 (Fig 4.9(b)). As L_c is

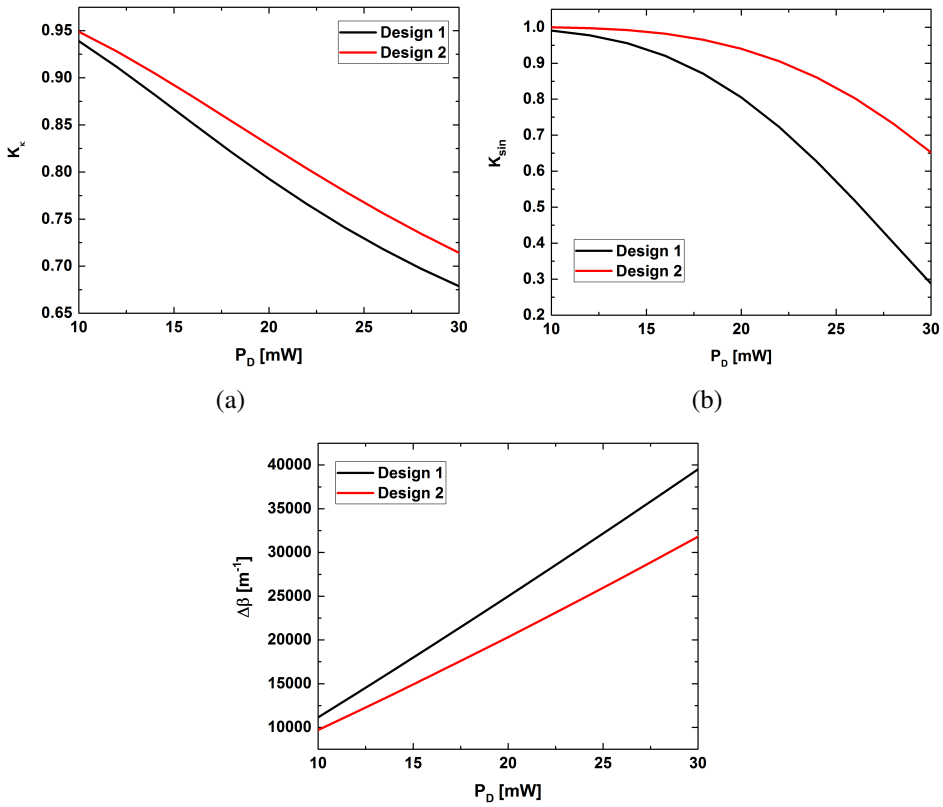

Figure 4.9: (a)Variation of K_{kappa} of both designs with P_D (b)Variation of K_{sin} of both designs with P_D(c)Variation of $\Delta\beta$ of both designs with P_D

constant, the fall in this component is completely dependent on $\Delta\beta$. From figure 4.9(c), we see that $\Delta\beta$ is indeed significantly greater for design 1. The change in κ is almost negligible (though it increases), compared to the $\Delta\beta$. This observation was also verified through simulations. From all the observations above we can conclude that $\Delta\beta$ is the dominating factor, but at the same time is lesser than or comparable to κ.

So, the proposed design has been shown to be superior to the previous design on the basis of it providing greater phase mismatch. This validates our design principle and corresponding optimizations carried out.

4.6 Losses due to mode mismatch in the design

We also have to consider the losses due to mode mismatch in our design i.e losses due to the mode profiles being different.First, we observe that there will be an interface between the region where the waveguide cross-section is as shown in Figure 4.10(a) and

h_{slab}	Value of overlap Integral	Loss (dB)
$130nm$	0.8481	$0.7155dB$
$50nm$	0.9905	$0.0415dB$

Table 4.4: Mode Mismatch Losses

where the waveguide cross-section is as shown in Figure 4.10(b) . This is because the complete etching is not executed everywhere, but is done only in the Coupling region. Since the modes in both the cross-sections will not overlap completely, insertion losses due to mode mismatch will be observed.

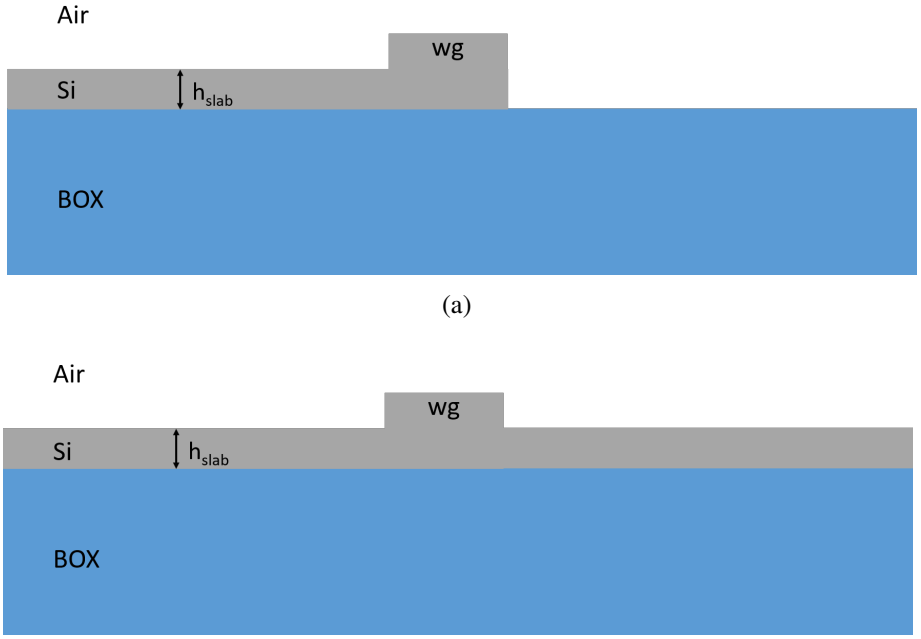

Figure 4.10: Schematic for the (a) cross section of the differentially etched region (b) cross section of the rib waveguide region

The mode mismatch loss is estimated by considering the mode overlap integral for the fundamental TE guided mode in the differentially etched waveguide and the fundamental TE mode in the rib waveguide. The values obtained are shown in the table 4.4. The modes in both the waveguide cross-sections are also simulated.The resulting mode profiles for which the overlap integral have to be computed are shown in Figure 4.10 for the case where $h_{slab} = 130nm$. For TE polarization, E_x is the dominant mode, so the E_x field intensity has been shown.

Note:For the coupled port, which is the port of interest, the total loss can be estimated

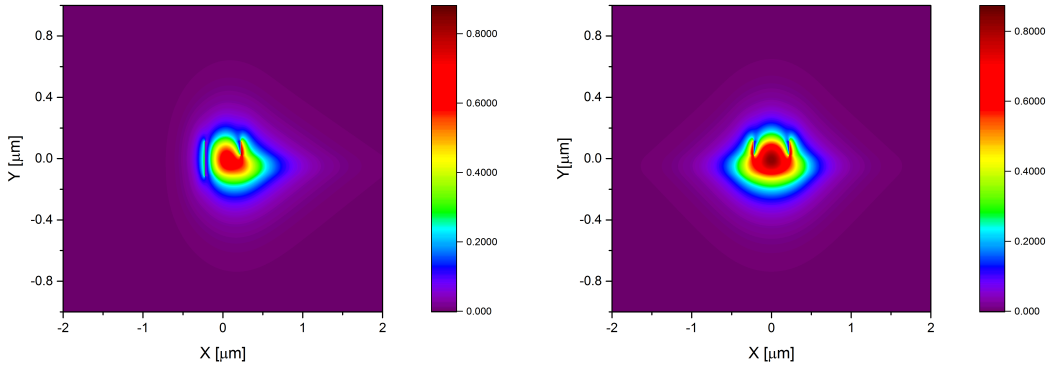

(a) (b)

Figure 4.11: Modal field strength (magnitude) profiles for (a) E_x of Fundamental TE mode (asymmetrically etched) (b) E_x of Fundamental TE mode (symmetrically etched) [$h_{slab} = 130nm$ and rib width=$450nm$]

by:

$$Loss_{total} = 2 * Loss_{modemismatch} + Loss_{heaterplacement}$$

4.7 Transient analysis of Thermal response

The transient analysis of the thermal response of the integrated design is of great importance since the rise time (τ_{rise}) for the thermal response is the limiting factor. This is based on the assumption that the optical response is much faster than the thermal response and can be considered to be instantaneous. Thus, the rise time of the Thermo-optic response is essentially the rise time of the Thermal response[19].It should be noted the heat transport equation is linear and time-invariant and therefore, the rise-time and fall-time of the device are equal.[19]

The rise time(τ_{rise}) indicates the time that a particular value of Temperature (at a point or average) takes to reach steady state value when a step input is given. Here, the step input is the heat flux applied to the heater. In particular, the rise time in our case is defined as the time taken for the particular value of temperature to rise from 0.05 times the steady state value to 0.95 times the steady state.The bounds taken for the rise time depend on the experimental conditions and requirements. Here the interval $[0.05 : 0.95]$ is taken to be the region of interest and consequently the bounds are 0.05 and 0.95. If the initial temperature is T_{ini} and the steady state temperature is T_{SS}, then rise time is

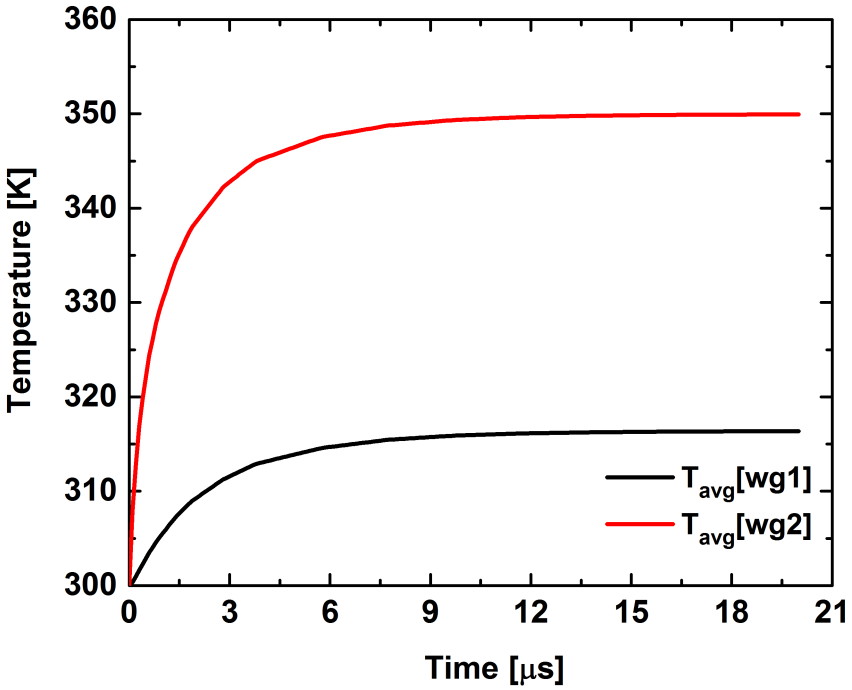

Figure 4.12: Transient response:Temperature vs time plot for both waveguide 1 and waveguide 2 [$P_D = 20mW$]; $T_{SS}[wg1] = 316.4$ and $T_{SS}[wg2] = 350$

defined as follows:

$$\tau_{rise} = t[T_{ini} + 0.05(\delta T) : T_{ini} + 0.95(\delta T)] \tag{4.3}$$

where $\delta T = T_{SS} - T_{ini}$ and $t[a : b]$ is the time taken for the temperature to change from a to b. The MATLAB function 'stepinfo()' was used to evaluate the rise times from the step responses.We also evaluate rise times for the average temperatures of the rib-waveguide cross-sections because the average temperature gives us a good understanding of the temperature changes in the waveguide regions [8]. While the midpoint of the waveguide was used as the point where the rise time was evaluated in [19], we verified that the rise times of the average and midpoint were very close and also posit that the rise time of the average temperature should give us a clearer picture of the trends.

The Temperature-time plots obtained from the Transient analyses for the average temperatures of waveguides 1 and 2 are shown in Figure 4.12. We notice from the plots that the steady state Temperature of Waveguide 2 is greater that of Waveguide 1. This follows from the fact that the waveguide 1 is farther from the heater and there is a

discontinuity in the heat transfer path (no intermediate slab region), so the heat has to pass to the waveguide 1 through the underlying BOX as shown in figure, leading to a large gradient [$33.6K$].

All the Transient Analyses are performed on COMSOL Multiphysics using the Solid-Heat Transfer module. The time dependent study is used to obtain the transient responses.The simulations on COMSOL and DEVICE match almost completely with a difference of the order of 0.1 or 0.01 K, possibly due to different meshing. This is expected since both the Simulation platforms are both Finite Element Method based and same boundary conditions are applied as mentioned in 2.3.2.

Transient studies allow us to examine the effect of configuration specifications and device parameters on the response times (estimated by rise time). The effect of three important parameters have been considered to extend the scope of our study and gain a deeper insight into heat transfer in our design.The 3 parameters are:

1. Thickness of the underlying BOX layer (t_{BOX})
2. Width of the heater (W_h)
3. Distance of the heater from the second waveguide (d)

A constant power of $P_D = 20mW$ is dissipated, since it is midway in the power range of our interest ($10mW - 30mW$). When one parameter is varied, the remaining parameters are kept constant. The results of the study are discussed for the $130nm$ slab height case since the trends will be the same for the device with $50nm$ case. This was also verified independently .

4.7.1 Variation of Rise time and Temperature gradient with Thickness of BOX under-clad

The thickness of the BOX is an important parameter to be considered, since it significantly affects both the rise time as well as the temperature profile/gradient of any SOI based design [19]. The variation of the rise time and and the Temperature gradient between the two waveguides is investigated by running a parameter sweep on COMSOL with the varying parameter set to be t_{BOX}. The minimum BOX thickness considered is

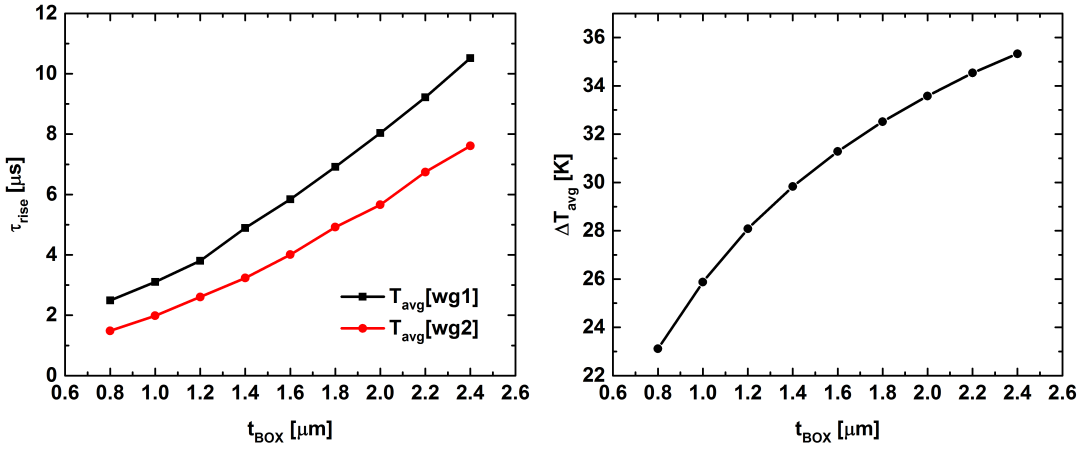

(a) (b)

Figure 4.13: (a) Variation of τ_{rise} with thickness of BOX (t_{BOX})(b) Variation of Temperature difference ($\Delta T_{avg} = T_{avg}(wg2) - T_{avg}(wg1)$) with thickness of BOX($t_{BOX}$) [$P_D = 20mW, h_{slab} = 130nm$]

$800nm$. This is set in order not to significantly degrade the device performance (device-Ring Resonator (RR)) specifically since TDC is generally used in conjunction with RR. The minimum BOX thickness required to keep the propagation loss below 0.08 dB/cm is around 700 nm [31].This is because a very small BOX thickness can cause leakage of the guided optical mode into the Si-underclad causing loss. The Temperature gradient is estimated as the difference between the average temperatures of both the waveguides. As mentioned, the remaining parameters (refer 4.1) are kept constant.

The variation of the rise times and Temperature gradients with varying BOX thicknesses can be seen in 4.13. Firstly we observe a significant difference between the rise times of waveguides 1 and 2. As mentioned earlier, this is because the waveguide 1 is father from the heater and is also separated from waveguide 2 by a discontinuity (air). This means that waveguide 1 will take significantly more time to reach steady state since heat has to pass through BOX(bad conductor of heat) in order to heat the first waveguide.

We also observe that as the BOX thickness increases, the rise times increase (for both waveguides) and so does the temperature gradient.This is because the underlying Si-underclad layer acts like a heat sink due to its very high thermal conductivity ($k(148W/mk)$) and large size(thickness= $3\mu m$). It is analogous to the role of a metal in electron transport.So, bringing the sink closer to the region of heat transfer means that

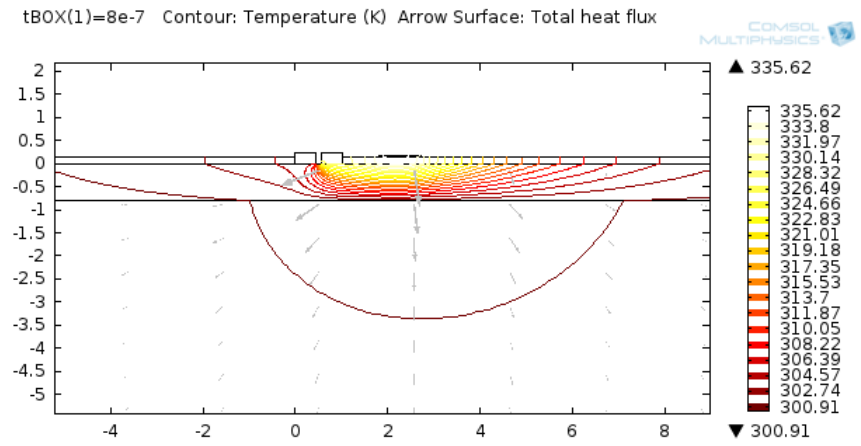

(a)

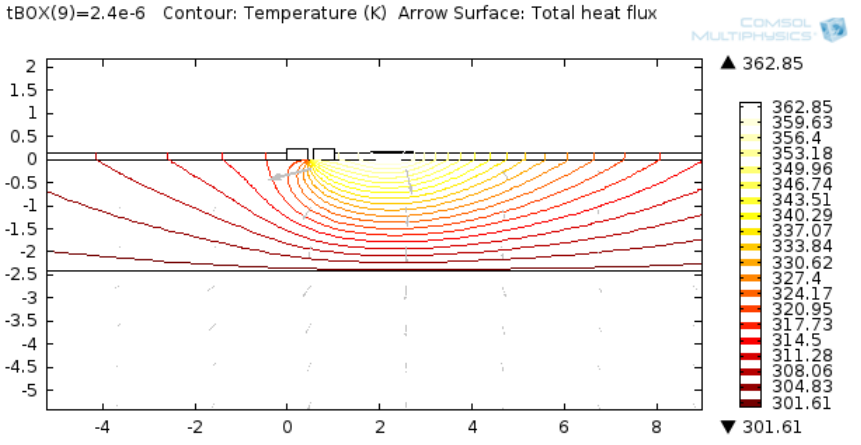

(b)

Figure 4.14: Temperature contour (Isothermal) profiles for (a) $t_{BOX} = 800nm$ (b) $t_{BOX} = 2.4\mu m$ $[d = 0.8\mu m, h_{slab} = 130nm]$

a larger amount of heat gets absorbed into the heat sink, thus decreasing the transverse temperature gradient. At the same time, the closer heat sink ensures that the steady state value is reached quicker since it stabilizes the Temperature profile faster. This explains the decrease in the rise time with decreasing BOX thickness. This can be seen from the Temperature-Contour/Isothermal plots for two different BOX thicknesses as shown in 4.14. We observe that the contour lines are more tightly bound in the BOX layer when the BOX thickness is lesser, further supporting the claim that the Si-underclad acts as a sink

Since, we are more interested in the Temperature gradient rather than the response time for the current design, we choose to maintain the value of $t_{BOX} = 2\mu m$ available in the lab as compared to the wafer with $t_{BOX} = 1\mu m$, as used in the design for a

thermo-optic phase-shifter mentioned in the paper [19].

4.7.2 Variation of Rise time and Temperature gradient with Heater width

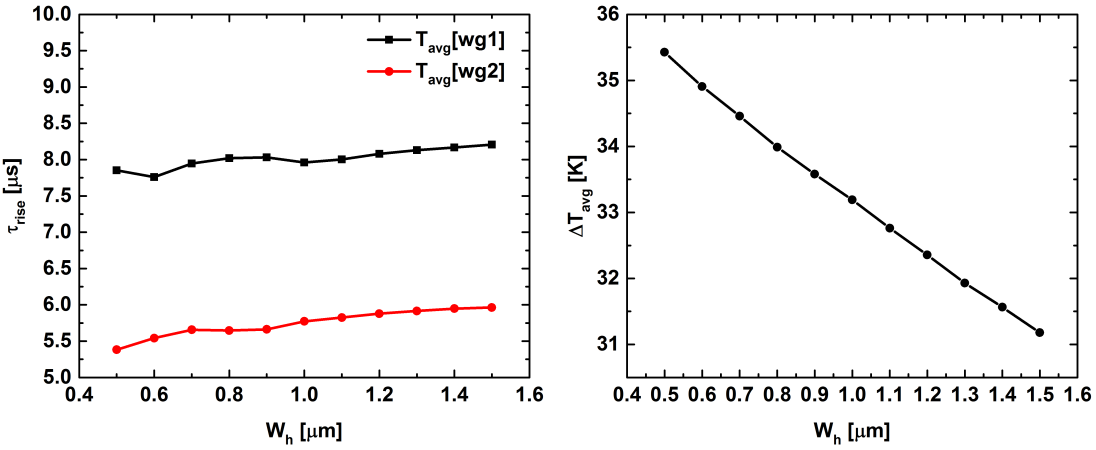

Figure 4.15: (a) Variation of τ_{rise} with width of the heater (W_h) (b) Variation of Temperature difference ($\Delta T_{avg} = T_{avg}(wg2) - T_{avg}(wg1)$) with the width of the heater (W_h) [$d = 0.8\mu m, h_{slab} = 130nm$]

Next, the effects of heater width (W_h) on the rise times (τ_{rise}) and the corresponding Temperature gradient are studied. From the figure 4.15, we observe that the rise times increase when the heater width is increased, but they increase by a very small amount. This is because as the width increases, the volume that is required to be heated also increases,leading to the increased rise times [19]. The temperature difference on the other hand, decreases when the waveguide width is increased. This is due to the increase in the area of cross-section when the width is increased. This means that the heat flux per unit area for the same power dissipated decreases, consequently leading to a lesser gradient.

It is observed from the temperature response of the micro-heater device (Figs. 4.15(a) and 4.15(b)),that the performance measures of such a device do not change considerably with the micro-heater width [$\Delta T = 5K, \tau_{rise}$ almost unchanged]. This is surprising, since the changes in the heater width (W_h) are directly reflected in the heat power flux applied to the heater. The heat power flux is the applied power/unit length divided

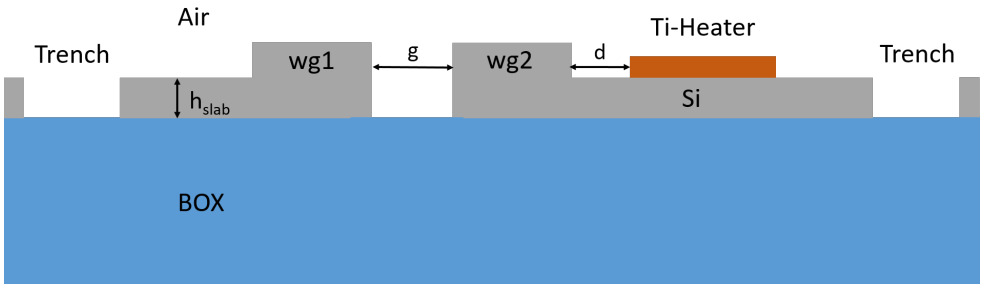

Figure 4.16: A schematic of the device cross-section with Trenches included

by the area of cross section. With the height kept constant, a change in width changes the cross section by the same amount i.e if the width is doubled, so is the area of cross-section. Thus, the variation in W_h in theory should affect the Temperature distribution significantly. But it is found not to be the case. This is mainly caused by the lateral diffusion of the heat in the cladding and BOX layers(approximately $1 - 2\mu m$ on each side of the micro-heater, here the distances will not be the same on either side) [32], which is comparable to the size of the micro-heater. Hence, to further reduce the heating volume, trenches can be etched on either side of the overall configuration as shown in Fig 4.16. The effect of the side trenches is significant in the performance of any thermo-optic device and can significantly decrease the heating volume and consequently the power consumption. The problem with this idea though, is that the rise times will increase significantly due to introduction of discontinuities (air trenches). This is possibly an area that requires more study and is another area for design-requirement based optimization.

4.7.3 Variation of Rise time and Temperature gradient with lateral separation between heater and DC region

Finally, the effects of the lateral separation of the metallic heater from the second waveguide on the rise times and Temperature gradients are studied.From the figure 4.17, we observe that as d increases, the rise times are not affected significantly but show a slight increase. This can explained by the hypothesis that farther the heater, the longer it will take for the temperatures at the waveguides to settle. It has already been observed that there is a lateral effect on the rise times, i.e the two different waveguides

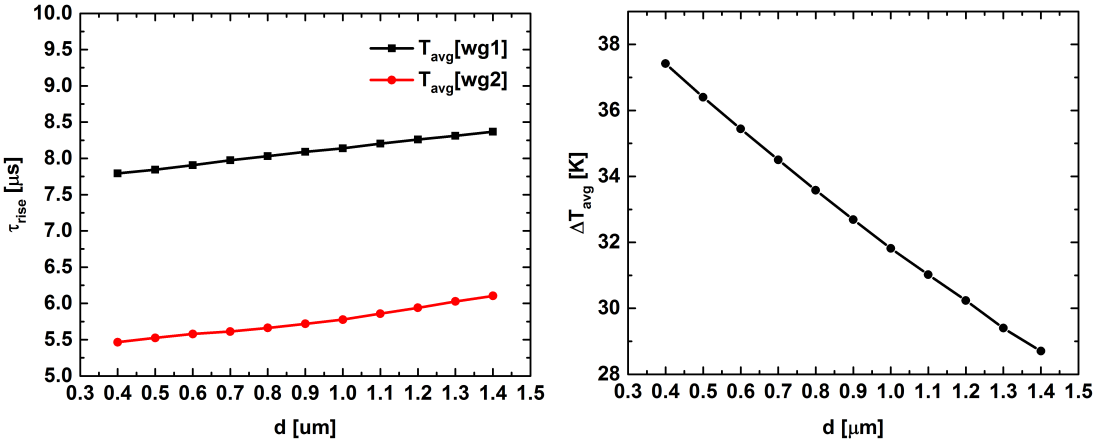

(a) (b)

Figure 4.17: (a) Variation of τ_{rise} with lateral separation of the heater(d)(b) Variation of Temperature difference ($\Delta T_{avg} = T_{avg}(wg2) - T_{avg}(wg1)$) with the lateral separation of the heater(d) [$W_h = 0.9\mu m, h_{slab} = 130nm$]

have different rise times of which the farther waveguide has a longer rise time. Essentially, farther the source, the greater the rise time. Extending this observation, we can explain that as d increases, rise times also increase.The observation that the heater distance (d) does not affect the rise times significantly means that d can be varied to improve the Tunability whilst maintaining the response time.

It is the temperature gradient that interests us from a modeling point of view. From figure 4.17(b), we see that as the distance (d) increases, the temperature difference (ΔT) decreases for the given geometric configuration. This is a very important observation, since it offers evidence that the Temperature difference is the main factor that affects Tunability. From figure 4.8, we see that the Tunability also decreases with increasing distance, i.e for the device with 130 nm slab height,$\Gamma[d = 0.8\mu m] > \Gamma[d = 1.2\mu m]$. The same trend is also followed for the device with 50 nm slab height,$\Gamma[d = 400nm] > \Gamma[d = 600nm]$. The temperature profiles for both cases were found to be similar. Thus,extending the observations made for the case where $h_{slab} = 130nm$, we can say that the temperature gradient increases with d and this is the principal cause for the tunability variance. This means that the heater should be placed as closely as possible for optimal device performance for any given slab height.

Design Specifications	$\tau_{rise}^{wg1}[\mu s]$	$\tau_{rise}^{wg2}[\mu s]$	$\Delta\tau[\mu s]$
With Over-clad ($d = 0.6\mu m$)	9.3926	8.5569	0.8357
Differentially etched ($g = 0.3\mu m and h_c = 80nm$)	6.7623	6.0476	0.7147
Final design ($d = 0.8\mu m and h_{slab} = 130nm$)	8.0326	5.6614	2.3712
Final design ($d = 0.8\mu m and h_{slab} = 50nm$)	7.6732	5.9944	1.6788

Table 4.5: Device parameters chosen for case 2 ($h_{slab} = 50nm$)

4.8 Comparison of rise times for the different models discussed

As mentioned earlier, the thermal response time is an important parameter for evaluating the device performance, since it gives us an idea of how quickly a device responds to an input.Though thermo-optic devices are slower than their plasma-optic counterparts, this does not allow for one to neglect the response time aspect of the device performance.The Table lists the rise times (τ_{rise}) of the average temperature in the first waveguides as well as the difference between the rise times of the waveguides ($\Delta\tau = \tau_{rise}^{wg1} - \tau_{rise}^{wg2}$) for the different designs discussed. The rise time for the first waveguide is considered since $\tau_{rise}^{wg1} > \tau_{rise}^{wg2}$. Thus, the rise time in waveguide 1 is the limiting factor and must be considered for estimating the response time of the overall device design.

The practical value of the response time for the overclad heater based design was found to be in the order of $10\mu s$[33],[8]. The value that we obtained through transient analysis was found to be 9.3926 (τ_{rise} of first waveguide is limiting value). So the time responses of the transient analysis was benchmarked. We see, that the differentially etched design has the least response times and the least difference in the rise times of waveguides among the designs considered. This is mainly because of the presence of Silicon with high thermal conductivity in the intermediate region. This ensures that there is a path of very low resistance for heat to the first waveguide, ensuring the quicker transfer and consequently quicker stabilization of waveguide1. On the other hand, the rise times of the final designs are lesser than the overclad-based models but only very slightly. They also have a greater difference between the rise times of the waveguides. This can be attributed to the presence of discontinuity or deep etching in the intermediate region. This means that the heat should travel through the BOX to the first waveguide, increasing the rise time as well as the $\Delta\tau$. The rise times are still lesser

than the overclad model because the volume that has to be heated is lesser. Comparing the final designs with both $h_{slab} = 130$ (case 1) and $h_{slab} = 50$ (case 2), we find that case 2 has a lower rise time but greater difference, though the difference between the models are almost insignificant. With respect to waveguide 2, since case 1 has a larger slab height, the rib is heated more and consequently it attains equilibrium faster as compare to case 2. For the observation of greater τ_{rise} in case 1, we hypothesize that for the waveguide 1, more heat fraction is injected into the BOX in case 2 and the heat is also less dissipated in case 2 (lower slab thickness, lesser conductivity and conductance). This means that waveguide 1 is exposed to more concentrated heat leading to quicker stabilization. The surprising thing about this observation is that even though case 2 has greater separation and greater gradient, the rise time is still smaller. Thus, the case 2which already had greater tunability seems to be a better overall design. We also see that the introduction of air gap reduces the extent to which the response time can be decreased. Though, the response times were lesser for the proposed design, the improvement over the overclad designs are not that large.

4.9 Concluding remarks

An 'Optically coupled but Thermally decoupled' design was proposed which showed much higher tunability based on its ability to create a larger gradient. Transient analysis was also carried out to obtain a better understanding of the rise times and heat transfer in the design. It was also estimated to have a marginally better response time than the overclad heater based design.

Two possible slab heights were considered and it was found that the design with the lesser slab height had better tunability,lower losses and better estimated response time. Though a device with 50nm slab height can be fabricated in principle, it is found that the grating coupler response is not good (noisy), at this slab height. The grating coupler is the basic component that couples light into the waveguide. Though lesser slab heights provide better performance on account of better modal confinement and greater gradient, the amount by which the slab height can be reduced depends on the available technology and the ease of fabrication. A two step E-beam process can be

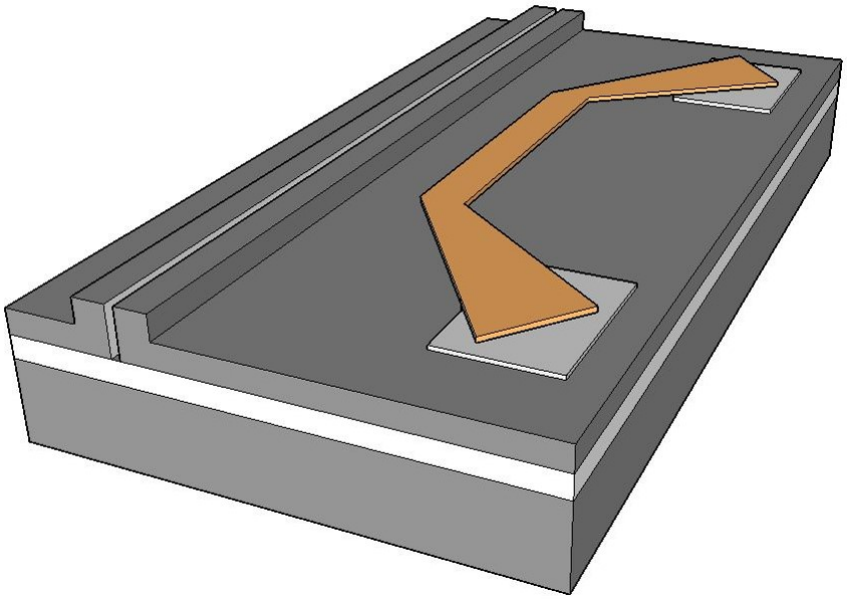

Figure 4.18: A 3-D schematic of the proposed device after fabrication

used to fabricate the aforementioned design due to the two slab heights required to be etched.The heater deposition (TI) can also be done after the first step using the lift off process. A 3-D representation of the proposed design has also been shown in figure 4.18.With respect to characterization, this design can be integrated with a ring resonator to experimentally study the tuning from the transmission response as has been done in [8]. Thus, the design for a compact TDC with greater tunability and lesser estimated response time was proposed and studied through simulations.

CHAPTER 5

Summary and future work

5.1 Summary

A two dimensional formulation was developed to numerically analyze Tunable directional coupler designs (submicron dimensions) by using translational symmetry. This formulation was benchmarked by using the said formulation on the TDC with over-clad. The simulation results were found to predict the trends correctly and also were concurrent with the experimental results at the optimal heater offset ($d = 0.6\mu m$).

In order to design a compact TDC with the heater parallely placed, a number of possible device designs were evaluated whilst also including phonon scattering effects and loss due to lateral offset of metal. Extending the idea of creating greater temperature difference/gradient to obtain better tuning, the concept of optically coupling the rib waveguides but thermally decoupling them by completely etching the intermediate region was proposed.

Following this concept, a compact tunable directional coupler without an over-clad was designed to obtain the maximum possible tunability (Γ),whilst being power efficient.The design was evaluated for two slab heights($h_{slab} = 50nm, 130nm$). Within the same intervals of power dissipated,tunabilities higher than those reported in [8] were obtained.The tunability was higher,the losses were less and the estimated response time was lesser for the case with lower slab height ($50nm$),though a setup is required to effectively fabricate and characterize the device at such low values of h_{slab}.All the simulations were done using MODE solutions,DEVICE and COMSOL multiphysics. The polarization considered was TE and the wavelength considered was $1.55\mu m$. Transient analyses were also performed on COMSOL to better understand the response times and comparisons with the existing design were also discussed. It was concluded from the transient analyses, that the proposed design is marginally faster compared to design with

overclad. It was also estimated that the response time of the proposed device would be less than $10\mu s$.

5.2 Future Work

The design and optimized structure needs to be fabricated on SOI platform using a two step E-beam lithography process.The fabricated structure, then needs to be characterized and tested. The effect of trenches on the device performance with regard to Tunability and response time need to studied to make the device more energy efficient whilst maintaining a good response time. Systematic 3-D simulations can also be used to compute the effect of the 'edge effects' on device performance and efforts should be made to decrease these 'edge effects' if they do have a significant impact on device performance. The wavelength dependence of the response should also be studied to get a more complete understanding of device performance.The device can be made more fabrication friendly and efforts can also be made to obtain a broadband response.

REFERENCES

[1] B. Jalali and S. Fathpour, "Silicon photonics," *Journal of lightwave technology*, vol. 24, no. 12, pp. 4600–4615, 2006.

[2] G. T. Reed, G. Mashanovich, F. Gardes, and D. Thomson, "Silicon optical modulators," *Nature photonics*, vol. 4, no. 8, pp. 518–526, 2010.

[3] A. Liu, R. Jones, L. Liao, D. Samara-Rubio, D. Rubin, O. Cohen, R. Nicolaescu, and M. Paniccia, "A high-speed silicon optical modulator based on a metal–oxide–semiconductor capacitor," *Nature*, vol. 427, no. 6975, pp. 615–618, 2004.

[4] Y. Vlasov, W. M. Green, and F. Xia, "High-throughput silicon nanophotonic wavelength-insensitive switch for on-chip optical networks," *nature photonics*, vol. 2, no. 4, pp. 242–246, 2008.

[5] P. Sun and R. M. Reano, "Submilliwatt thermo-optic switches using free-standing silicon-on-insulator strip waveguides," *Optics express*, vol. 18, no. 8, pp. 8406–8411, 2010.

[6] N. C. Harris, Y. Ma, J. Mower, T. Baehr-Jones, D. Englund, M. Hochberg, and C. Galland, "Efficient, compact and low loss thermo-optic phase shifter in silicon," *Optics express*, vol. 22, no. 9, pp. 10 487–10 493, 2014.

[7] K. Suzuki, K. Tanizawa, T. Matsukawa, G. Cong, S.-H. Kim, S. Suda, M. Ohno, T. Chiba, H. Tadokoro, M. Yanagihara *et al.*, "Ultra-compact $8\times$ 8 strictly-non-blocking si-wire piloss switch," *Optics express*, vol. 22, no. 4, pp. 3887–3894, 2014.

[8] P. Orlandi, F. Morichetti, M. J. Strain, M. Sorel, A. Melloni, and P. Bassi, "Tunable silicon photonics directional coupler driven by a transverse temperature gradient," *Optics letters*, vol. 38, no. 6, pp. 863–865, 2013.

[9] P. Dong, W. Qian, H. Liang, R. Shafiiha, N.-N. Feng, D. Feng, X. Zheng, A. V. Krishnamoorthy, and M. Asghari, "Low power and compact reconfigurable multiplexing devices based on silicon microring resonators," *Optics express*, vol. 18, no. 10, pp. 9852–9858, 2010.

[10] P. Dong, N.-N. Feng, D. Feng, W. Qian, H. Liang, D. C. Lee, B. Luff, T. Banwell, A. Agarwal, P. Toliver *et al.*, "Ghz-bandwidth optical filters based on high-order silicon ring resonators," *Optics express*, vol. 18, no. 23, pp. 23 784–23 789, 2010.

[11] H. Kogelnik and R. V. Schmidt, "Switched directional couplers with alternating $\delta\beta$," *IEEE Journal of Quantum Electronics*, vol. 12, no. 7, pp. 396–401, 1976.

[12] J. Leuthold and C. Joyner, "Multimode interference couplers with tunable power splitting ratios," *Journal of lightwave technology*, vol. 19, no. 5, pp. 700–707, 2001.

[13] M. S. Rasras, K.-Y. Tu, D. M. Gill, Y.-K. Chen, A. E. White, S. S. Patel, A. Pomerene, D. Carothers, J. Beattie, M. Beals *et al.*, "Demonstration of a tunable microwave-photonic notch filter using low-loss silicon ring resonators," *Journal of Lightwave Technology*, vol. 27, no. 12, pp. 2105–2110, 2009.

[14] L.-W. Luo, S. Ibrahim, A. Nitkowski, Z. Ding, C. B. Poitras, S. B. Yoo, and M. Lipson, "High bandwidth on-chip silicon photonic interleaver," *Optics express*, vol. 18, no. 22, pp. 23 079–23 087, 2010.

[15] M. Tran, J. Hulme, S. Srinivasan, J. Peters, and J. Bowers, "Demonstration of a tunable broadband coupler," in *Photonics Conference (IPC), 2015*. IEEE, 2015, pp. 488–489.

[16] J. Van Campenhout, W. M. Green, S. Assefa, and Y. A. Vlasov, "Integrated nisi waveguide heaters for cmos-compatible silicon thermo-optic devices," *Optics Letters*, vol. 35, no. 7, pp. 1013–1015, 2010.

[17] M. R. Watts, J. Sun, C. DeRose, D. C. Trotter, R. W. Young, and G. N. Nielson, "Adiabatic thermo-optic mach–zehnder switch," *Optics letters*, vol. 38, no. 5, pp. 733–735, 2013.

[18] R. K. Endo, Y. Fujihara, and M. Susa, "Calculation of the density and heat capacity of silicon by molecular dynamics simulation," *High Temp High Press*, vol. 35, no. 36, pp. 505–511, 2003.

[19] A. Atabaki, E. S. Hosseini, A. Eftekhar, S. Yegnanarayanan, and A. Adibi, "Optimization of metallic microheaters for high-speed reconfigurable silicon photonics," *Optics express*, vol. 18, no. 17, pp. 18 312–18 323, 2010.

[20] X. Wang, J. A. Martinez, M. S. Nawrocka, and R. R. Panepucci, "Compact thermally tunable silicon wavelength switch: Modeling and characterization," *IEEE Photonics Technology Letters*, vol. 20, no. 11, pp. 936–938, 2008.

[21] C. Sujith, "Integrated optical microring resonator in soi for wide range refractive index sensing," Ph.D. dissertation, Indian Institute of Technology Madras, 2016.

[22] A. Yariv and P. Yeh, *Photonics: Optical Electronics in Modern Communications*. Oxford University Press, 2006.

[23] J. M. Jewell, "Thermooptic coefficients of some standard reference material glasses," *Journal of the American Ceramic Society*, vol. 74, no. 7, pp. 1689–1691, 1991.

[24] G. Cocorullo, F. Della Corte, and I. Rendina, "Temperature dependence of the thermo-optic coefficient in crystalline silicon between room temperature and 550 k at the wavelength of 1523 nm," *Applied physics letters*, vol. 74, no. 22, pp. 3338–3340, 1999.

[25] Y. S. Ju, "Phonon heat transport in silicon nanostructures," *Applied Physics Letters*, vol. 87, no. 15, p. 153106, 2005.

[26] A. Rohatgi, "WebPlotDigitizer," http://arohatgi.info/WebPlotDigitizer, June, 2017, [Online; accessed 9-June-2017].

[27] P. Leturcq, J.-M. Dorkel, A. Napieralski, and E. Lachiver, "A new approach to thermal analysis of power devices," *IEEE Transactions on Electron Devices*, vol. 34, no. 5, pp. 1147–1156, 1987.

[28] X. Wang and B. Huang, "Computational study of in-plane phonon transport in si thin films," *Scientific reports*, vol. 4, p. 6399, 2014.

[29] S. Kaushal, "Modelling and Experimental Investigation of an Integrated Optical Microheater in SOI," Master's thesis, Indian Institute of Technology Madras, India, 2016.

[30] M. edu, "PVD Titanium," http://www.mit.edu/~6.777/matprops/titanium.htm, June, 2017, [Online; accessed 9-June-2017].

[31] M. Popović, "Theory and design of high-index-contrast microphotonic circuits," Ph.D. dissertation, Massachusetts Institute of Technology, 2008.

[32] A. A. Bilotti, "Static temperature distribution in ic chips with isothermal heat sources," *IEEE Transactions on Electron Devices*, vol. 21, no. 3, pp. 217–226, 1974.

[33] A. Melloni, A. Canciamilla, C. Ferrari, F. Morichetti, L. O'Faolain, T. Krauss, R. De La Rue, A. Samarelli, and M. Sorel, "Tunable delay lines in silicon photonics: coupled resonators and photonic crystals, a comparison," *IEEE Photonics Journal*, vol. 2, no. 2, pp. 181–194, 2010.